9-2020

THE ELECTRONIC PROPERTIES OF THE QUASI-ONE-DIMENSIONAL TRANSITION METAL TRICHALCOGENIDES: TiS_3 AND ZrS_3

Simeon Gilbert
University of Nebraska-Lincoln, simeon.gilbert@outlook.com

THE ELECTRONIC PROPERTIES OF THE QUASI-ONE-DIMENSIONAL TRANSITION METAL TRICHALCOGENIDES: TiS_3 AND ZrS_3

by

Simeon James Gilbert

A DISSERTATION

Presented to the Faculty of

The Graduate College at the University of Nebraska

In Partial Fulfilment of Requirements

For the Degree of Doctor of Philosophy

Major: Physics and Astronomy

Under the Supervision of Peter A. Dowben

Lincoln, Nebraska

September, 2020

THE ELECTRONIC PROPERTIES OF THE QUASI-ONE-DIMENSIONAL TRANSITION METAL TRICHALCOGENIDES: TiS_3 AND ZrS_3

Simeon J. Gilbert, Ph.D.

University of Nebraska, 2020

Advisor: Peter A. Dowben

The transition metal trichalcogenides are a class of materials formed by 1D chains of covalently bound MX_3 (M=Ti, Zr, Hf, Ta, Nb; X=S, Se, Te) trigonal prisms which are held together by weak van der Waals forces to form 2D sheets. Because of their superior edge termination, these materials suppress edge scattering effects that plague other two-dimensional materials thus enabling devices scaling to widths below 10 nm. Furthermore, this quasi-one-dimensional structure results in highly anisotropic electronic and optical properties which were examined through angle resolved photoemission spectroscopy and scanning photocurrent microscopy. These measurements show that the hole carrier masses are drastically altered along different in-plane crystallographic directions and that the photocurrent production in these materials is strongly dependent on the polarization of the exciting light. Angle resolved photoemission spectroscopy and X-ray absorption spectroscopy indicate that TiS_3 and ZrS_3 exhibit strong metal-sulfur hybridization within both the conduction and valence bands. A combination of X-ray photoemission spectroscopy and device measurements were utilized to show that strong bonding with the surface sulfur atoms in TiS_3 prevents Schottky barrier formation with Au and Pt metal contacts. Furthermore, there are indications from both scanning photocurrent microscopy and X-ray magnetic circular dichroism measurements that these materials can support symmetry protected spin-polarized currents which could be utilized to create spintronic devices. When these findings are combined with the transition metal trichalcogenides' superior edge termination, it becomes clear that these materials are promising for various applications in the fields of nanoelectronics, optoelectronics, and spintronics.

ACKNOWLEDGEMENTS

First and foremost, I would like to thank my advisor Dr. Peter Dowben for providing direction for my dissertation research, facilitating numerous collaborations, and working tirelessly to ensure funding and resources all of which were necessary for the timely completion of my graduate studies.

I am extremely appreciative of Dr. Elena Echeverría and Dr. Takashi Koemsu for their guidance in learning various ultra-high vacuum and photoemission techniques that have been indispensable throughout my graduate career. I would also like to thank Dr. Andrew Yost for numerous discussions regarding both fundamental physics and experimental techniques which contributed to the success of my research.

I am both indebted and grateful to Dr. Alexey Lipatov and Dr. Alexander Sinitskii for providing the high quality crystals which made this dissertation research possible. A large portion of this work was completed at the Synchrotron SOLEIL and could not have been accomplished without the help of Dr. Maria Asensio, Dr. Jose Ávila, and Dr. Hemian Yi. This work was also significantly improved by comparison to theory calculations which were provided by Dr. Tula Paudel and Dr. Evgeny Tsymbal. I would also like to thank Dr. Jian Wang from the Canadian Light Source for his instruction in photoemission electron microscopy and his willingness to take additional measurements.

I would like to express my gratitude to my committee members: Dr. Alexander Sinitskii, Dr. Christian Binek, and Dr. Xiaoshan Xu for their assistance and advice in my dissertation work.

Finally, I would like to thank my wife Sabra Gilbert for sharing in the numerous joys, struggles, and disappointments which have led to this point and for making this journey worthwhile.

PREFACE

The findings in Chapter 3 have been published in:

> H. Yi, T. Komesu, S. Gilbert, G. Hao, A. J. Yost, A. Lipatov, A. Sinitskii, J. Avila, C. Chen, M. C. Asensio and P. A. Dowben, "The Band Structure of the Quasi-One-Dimensional Layered Semiconductor TiS_3(001)," *Appl. Phys. Lett.* **112**, 052102 (2018).
>
> and
>
> H. Yi, S. J. Gilbert, A. Lipatov, A. Sinitskii, J. Avila, J. Abourahma, T. Komesu, M. C. Asensio, and P. A. Dowben, "The electronic band structure of quasi-one-dimensional van der Waals semiconductors: the effective hole mass of ZrS_3 compared to TiS_3," *J. Phys.: Condens. Matter* **32**, 29LT01 (2020).

Chapter 4 has been published in:

> S. J. Gilbert, H. Yi, J-S Chen, A.J. Yost, A. Dhingra, J. Abourahma, A. Lipatov, J. Avila, T. Komesu, A. Sinitskii, M. C. Asensio, and P. A. Dowben, "The Effect of Band Symmetry on Photocurrent Production in the Quasi-One-Dimensional Transition Metal Trichalcogenides," *ACS Appl. Mater. Interfaces* **12**, 40525 (2020).

Chapter 5 has been submitted for publication in:

> S. J. Gilbert, H. Yi, A. Lipatov, A. J. Yost, T. Komesu, A. Sinitskii, J. Avila, M. C. Asensio, and P. A. Dowben, "Strong Metal-Sulfur Hybridization in the Conduction Band of the Quasi-One-Dimensional Transition Metal Trichalcogenides: TiS_3 and ZrS_3," Submitted to J. Phys. Chem. C

The findings in Chapter 6 have been published in:

> S. J. Gilbert, A. Lipatov, A. J. Yost, M. J. Loes, A. Sinitskii, and P. A. Dowben, "The electronic properties of Au and Pt metal contacts on quasi-one-dimensional layered TiS_3(001)," *Appl. Phys. Lett.* **114**, 101604 (2019).

Portions of the discussion on Chapter 7 were taken from:

> S. J. Gilbert and P. A. Dowben, "Direct Measurements of Proximity Induced Spin Polarization in 2D Systems," *J. Phys. D: Appl. Phys.* **53**, 343001 (2020).
>
> and
>
> S. J. Gilbert, M. Li, J-S Chen, H. Yi, A. Lipatov, J. Avila, A. Sinitskii, M. C. Asensio, P. A. Dowben, and A. J. Yost, "Symmetry Protected Photocurrent in a Quasi-1-D TiS_3 (001) Phototransistor," in preparation

Table of Contents

1. Introduction

Transition metal trichalcogenides (TMTs) have garnered increased attention from researchers in recent years for possible applications in electronics [1-7], optoelectronics [1,8-18], thermoelectrics [19-22] and energy storage [23-26]. The TMTs are notable for their quasi-one-dimensional (1D) structure [27], which comprises 1D chains of covalently bonded MX_3 (M= Ti, Zr, Hf, Ta, Nb; X=S, Se, Te) trigonal prisms assembled into two-dimensional (2D) sheets by means of weak van der Waals-like bonding which is shown for TiS_3 in Figure 1.1(a) [28]. Because of their quasi-1D structure, TMT crystals typically grow in the form of needle-like crystals [Figure 1(b)] with their long axes along the crystallographic b direction of 1D chains, as indicated by the transmission electron microscopy (TEM) image in Figure 1.1(c). Similar to other 2D materials, these whiskers can be mechanically exfoliated into few-layer or even monolayer crystals [28]. The TMTs are favored over other 2D materials because the quasi-1D TMTs have edge terminations and edge charge accumulation that may ameliorate or suppress detrimental edge scattering effects [27,28]. By way of comparison, 2D materials such as graphene and transition metal dichalcogenides experience significant edge scattering effects in sub-10 nm devices, as is evident in both theory [29-32] and experiment [33-35]. The smallest structural unit of the TMTs, a 1D chain of MX_3 prisms [Figures 1.1(a) and 1.1(c)], is atomically smooth and free from dangling bonds or stabilizing functional groups, which significantly reduces the number of edge defects compared to the rough edges of patterned or exfoliated 2D materials.

The transport within the 2D plane of these TMTs is also highly anisotropic resulting in preferential charge transport along the chain direction, while minimizing edge scattering [2,27]. There has been a flurry of effort to calculate the band structure of TiS_3 not only because of its highly anisotropic crystal structure [2,36-39] but also because of the search for alternative electrode materials [25]. While recently transistors have been made using TiS_3 as the channel material [1,2,4,5,10,25,40], the measured mobility was low (80 $cm^2 V^{-1} s^{-1}$ or less at room temperature), but

contact issues are well known to lower the measured mobility in 2D material field effect transistors. Thus, the effective mass along the chain direction is a key parameter and experimental confirmation is essential to assess the efficacy of this class of trichalcogenides as a 2D semiconductor transport layer.

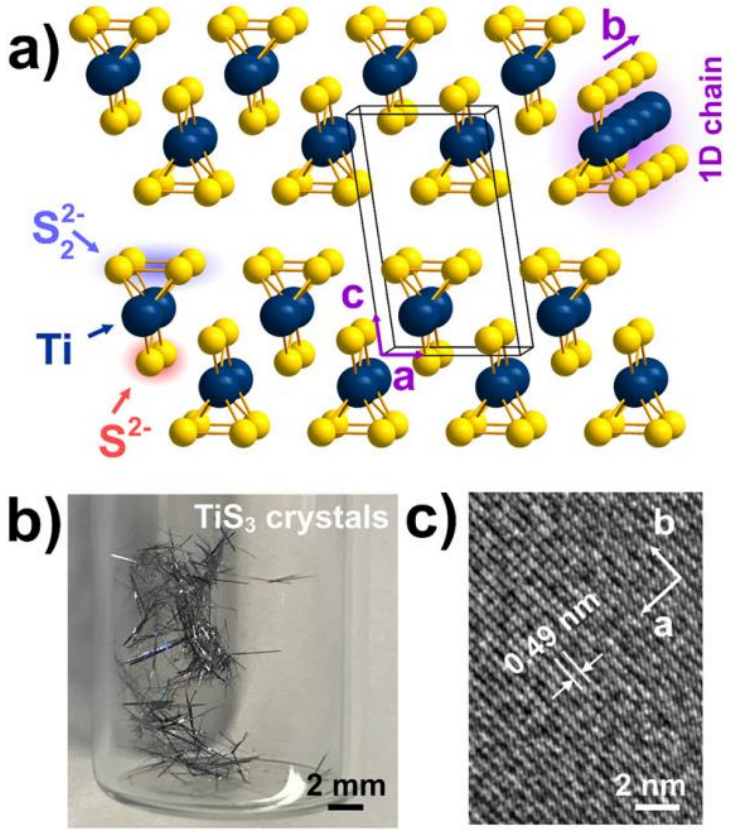

Figure 1.1 *(a) A schematic of the monoclinic TiS_3 crystal structure with a $P2_1/m$ space group. (b) Optical photograph of TiS_3 crystals. (c) High-resolution TEM image of the 1D chains oriented along the b crystallographic direction in TiS_3 crystals. The image was recorded using a FEI Tecnai Osiris scanning transmission electron microscope at the accelerating voltage of 200 kV. Data taken by Alexey Lipatov. Figure published in S. J. Gilbert, A. Lipatov, A. J. Yost, M. J. Loes, A. Sinitskii, and P. A. Dowben, Appl. Phys. Lett.* ***114****, 101604 (2019).*

Higher Z value TMTs are expected to exhibit significant spin–orbit coupling [41,42] which is desirable for the next generation of spintronic devices [43-46]. For such devices, ZrS_3 and HfS_3 would be far more desirable, as the spin–orbit coupling is expected to be more significant than TiS_3. The question is then whether the TiS_3 n-type character and low effective carrier mass (hence high mobility) is retained in ZrS_3 and HfS_3. Despite this, research on the electronic properties and band structure of higher Z value TMTs is far from complete [41]. In the case of ZrS_3, there are a handful of theoretical band structure calculations [9,16,37,47,48]. Chapter 3 is directed towards establishing the experimental band structure for both TiS_3(001) and ZrS_3(001).

The transition metal trichalcogenides are also set apart from other 2D materials by their strongly anisotropic optical and electronic properties within their 2D layers [1,8,9,27,49,50]. Of particular interest are the strongly light polarization dependent optical properties which have been demonstrated for both TiS_3 and ZrS_3 [1,8,9,16,18,51-52]. The polarization dependent optical properties are promising for the creation of polarization sensitive photodetectors. Photocurrent measurements, in previous studies, have shown dichroic ratios as high as 4:1 for TiS_3 [8] and 2.55:1 for ZrS_3 [9], and the dichroic ratio has been reported to depend on both the excitation energy [1,8,9] and sample thickness [9,50]. Although established experimentally, the underlying mechanisms at play in this photocurrent production have not been intensely studied. In Chapter 4, we show that these effects are the result of electronic orbital symmetry by comparing polarization dependent scanning photocurrent microscopy (SPCM) to polarization dependent nanospot angle resolved photoemission spectroscopy (nanoARPES) for both TiS_3 and ZrS_3.

As a semiconductor, TiS_3 is generally n-type [2,3,4,5,6,19,27,53], with potentially extremely light mass carriers [36], where the conduction band edge is low lying enough with respect to the Fermi level that with sufficient gate voltage, the TiS_3 can be driven through a nonmetal to metal transition [6]. So, investigations into the electronic structure of the conduction band are extremely important to better understand the majority carrier transport. Detailed

investigations into the conduction band orbital hybridization in the transition metal trichalcogenides like TiS_3 [54-56] and ZrS_3 [57] remain sparse, nonetheless. In Chapter 5, we provide insight into the unoccupied electron states of two TMTs, TiS_3 and ZrS_3, through a comparison of X-ray absorption spectroscopy (XAS) and density functional theory (DFT) which indicates that the conduction band structure, near the Fermi level of both materials, is composed largely of p-d hybridized orbitals.

Among the various transition metal trichalcogenides, TiS_3 shows exceptional promise due to its favorable band gap (~1 eV) and predicted high electron mobility (~10,000 $cm^2\ V^{-1}\ s^{-1}$) [36] for a monolayer sheet. However, the experimentally measured mobility of few-layer TiS_3 FETs has never exceeded 100 $cm^2\ V^{-1}\ s^{-1}$ and remains two orders of magnitude below predictions [1,2,4,5,40]. This discrepancy is not surprising as the first graphene field-effect transistors had mobilities of a few hundred $cm^2\ V^{-1}\ s^{-1}$, which was improved to over 100,000 $cm^2\ V^{-1}\ s^{-1}$ with proper device optimization [58,59]. Recently, phonon scattering has been implicated in the reduction of electron mobility in TiS_3 [6], but another explanation for low electron mobility is the formation of a Schottky barrier which has inhibited the performance of other 2D materials [2,60], Previous experiments on TiS_3 have utilized Cr/Au [4,6] or Ti/Au [1,2,5] contacts, with the Ti/Au contacts exhibiting evidence of a Schottky barrier [2], while the Cr/Au contacts seem to create Ohmic contacts [4,6]. In both cases, Au was not the direct contact metal with TiS_3. Higher work function metals, such as Au, are generally expected to form larger Schottky barriers on n-type semiconductors [61], such as TiS_3 [27]. This trend has previously been observed for 2D MoS_2 [60]. In Chapter 6, we studied the interface between TiS_3 and the high work function metals Au and Pt by means of X-ray photoemission spectroscopy (XPS) and electrical transport measurements of TiS_3 FETs

Finally, in Chapter 7, the potential of using these quasi-1D materials coupled with an antiferromagnetic substrate will be discussed. It was shown by Dzhioev et al. [62] that the electron spins in a semiconductor, at the interface with a ferromagnet, experience an additional spin

relaxation which depends upon the ferromagnet's magnetization. This interaction, known as the proximity effect, could be used to spin polarize the electrons within a 2D transistor channel to create a 2D spin field-effect transistor [43,44,46,63-67]. Furthermore, utilizing the proximity effect at the interface with a magnetoelectric antiferromagnet with net boundary magnetization, such as Cr2O3 [67-72], would provide voltage controlled magneto-electric switching in MTJs [46,64,73-76], antiferromagnetic spin-orbit read (AFSOR) logic [43-46,63], and spin FETs [43,44,46,63,64]. Devices based on this antiferromagnetic switching would offer substantial advantages in switching speed and power consumption over ferromagnetic spintronic devices [44,46].

References

[1] J. O. Island, R. Biele, M. Barawi, J. M. Clamagirand, J. R. Ares, C. Sánchez, H. S. J. Van Der Zant, I. J. Ferrer, R. D'Agosta, and A. Castellanos-Gomez, *Sci. Rep.* **6**, 22214 (2016).

[2] J. O. Island, M. Barawi, R. Biele, A. Almazán, J. M. Clamagirand, J. R. Ares, C. Sánchez, H. S. J. Van Der Zant, J. V. Álvarez, R. D'Agosta, I. J. Ferrer, and A. Castellanos-Gomez, *Adv. Mater.* **27**, 2595 (2015).

[3] S. J. Gilbert, A. Lipatov, A. J. Yost, M. J. Loes, A. Sinitskii, and P. A. Dowben, *Appl. Phys. Lett.* **114**, 101604 (2019).

[4] A. Lipatov, P. M. Wilson, M. Shekhirev, J. D. Teeter, R. Netusil, and A. Sinitskii, *Nanoscale* **7**, 12291 (2015).

[5] A. J. Molina-Mendoza, J. O. Island, W. S. Paz, J. M. Clamagirand, J. R. Ares, E. Flores, F. Leardini, C. Sánchez, N. Agraït, G. Rubio-Bollinger, H. S. J. van der Zant, I. J. Ferrer, J. J. Palacios, and G. Castellanos-Gomez, *Adv. Funct. Mater.* **27**, 1605647 (2017).

[6] M. Randle, A. Lipatov, A. Kumar, C-P Kwan, J. Nathawat, B. Barut, S. Yin, K. He, N. Arabchigavkani, R. Dixit, T. Komesu, J. Avila, M. C. Asensio, P. A. Dowben, A. Sinitskii, U. Singisetti, and J. P. Bird, *ACS Nano* **13,** 803 (2018).

[7] W-W Xiong, J-Q Chen, X-C Wu, and J-J Zhu, *J. Mater. Chem. C* **2**, 7392 (2014).

[8] S. Liu, W. Xiao, M. Zhong, L. Pan, X. Wang, H-X Deng, J. Liu, J. Li, and Z. Wei, *Nanotechnology* **29**, 184002 (2018).

[9] X. Wang, K. Wu, M. Blei, Y. Wang L. Pan, K. Zhao, C. Shan, M. Lei, Y. Cui, B. Chen, D. Wright, W. Hu, S. Tongay, and Z. Wei, *Adv. Electron. Mater.* **5**, 1900419 (2019).

[10] J. O. Island, M. Buscema, M. Barawi, J. M. Clamagirand, J. R. Ares, C. Sánchez, I. J. Ferrer, G. A. Steele, H. S. J. van der Zant, and A. Castellanos-Gomez, *Adv. Opt. Mater.* **2**, 641 (2014).

[11] I. J. Ferrer, M. D. Maciá, V. Carcelén, J. R. Ares, and C. Sánchez, *Energy Procedia* **22**, 48 (2011).

[12] Q. Cui, A. Lipatov, J. S. Wilt, M. Z. Bellus, X. C. Zeng, J. Wu, A. Sinitskii, and H. Zhao, *ACS Appl. Mater. Interfaces* **8**, 18334 (2016).

[13] I. J. Ferrer, J. R. Ares, J. M. Clamagirand, M. Barawi, and C. Sánchez, *Thin Solid Films* **535**, 398 (2013).

[14] Y. Niu, R. Frisenda, E. Flores, J. R. Ares, W. Jiao, D. Perez de Lara, C. Sánchez, R. Wang, I. J. Ferrer, and A. Castellanos-Gomez, *Adv. Opt. Mater.* **6**, 1800351 (2018).

[15] M. Talib, R. Tabassum, Abid, S. S. Islam, and P. Mishra, *ACS Omega* **4**, 6180 (2019).

[16] A. Pant, E. Torun, B. Chen, S. Bhat, X. Fan, K. Wu, D. P. Wright, F. M. Peeters, E. Soignard, H. Sahin, and S. Tongay, *Nanoscale* **8**, 16259 (2016).

[17] T. R. Tao, J. J. Wu, and X. C. Wu, *Nanoscale* **7**, 14292 (2015).

[18] S. Yang, M. Wu, W. Shen, L. Huang, S. Tongay, K. Wu, B. Wei, Y. Qin, Z. Wang, C. Jiang, and C. Hu, *ACS Appl. Mater. Interfaces* **11**, 3342 (2019).

[19] N. V. Morozova, I. V. Korobeinikov, K. V. Kurochka, A. N. Titov, and S. V. Ovsyannikov, *J. Phys. Chem. C* **122**, 14362 (2018).

[20] T. Sakuma, S. Nishino, M. Miyata, and M. Koyano, *J. Electron. Mater.* **47**, 3177 (2018).

[21] E. Guilmeau, D. Berthebaud, P. R. N. Misse, S. Hébert, O. I. Lebedev, D. Chateigner, C. Martin, and A. Maignan, *Chem. Mater.* **26**, 5585 (2014).

[22] J. Zhang, X. Liu, Y. Wen, L. Shi, R. Chen, H. Liu, and B. Shan, *ACS Appl. Mater. Interfaces* **9**, 2509 (2017).

[23] N. Tanibata, T. Matsuyama, A. Hayashi, and M. J. Tatsumisago, *Power Sources* **275**, 284 (2015).

[24] Y. Liu, J. Lian, and X. Yang, *Applied Physics Express* **9**, 011801 (2016).

[25] M. Arsentev, A. Missyul, A. V. Petrov, and M. J. Hammouri, *Phys. Chem. C* **121**, 15509 (2017).

[26] J. Wu, D. Wang, H. Liu, W-M Lau, and L-M Liu, *RSC Adv.* **5**, 21455 (2015).

[27] H. Yi, T. Komesu, S. Gilbert, G. Hao, A. J. Yost, A. Lipatov, A. Sinitskii, J. Avila, C. Chen, M. C. Asensio, and P. A. Dowben, *Appl. Phys. Lett.* **112**, 052102 (2018).

[28] A. Lipatov, M. J. Loes, H. Lu, J. Dai, P. Patoka, N. S. Vorobeva, D. S. Muratov, G. Ulrich, B. Kastner, A. Hoehl, G. Ulm, X. C. Zeng, E. Ruhl, A. Gruverman, P. A. Dowben, and A. Sinitskii, *ACS Nano* **12**, 12713 (2018)

[29] E. R. Mucciolo and C. H. Lewenkopf, *J. Phys.: Condens. Matter* **22**, 273201 (2010)

[30] J. Wurm, K. Richter, and I. Adagideli, *Phys. Rev. B* **84**, 075468 (2011).

[31] V. K. Dugaev and M. I. Katsnelson, *Phys. Rev. B* **88**, 235432 (2013).

[32] M. Wimmer, I. Adagideli, S. Berber, D. Tomanek, and K. Richter, *Phys. Rev. Lett.* **100**, 177207 (2008).

[33] Y. Yang and R. Murali, *IEEE Electron Device Lett.* **31**, 237 (2010).

[34] M. Y. Han, J. C. Brant, and P. Kim, *Phys. Rev. Lett.* **104**, 056801 (2010).

[35] Y.-J. Shi, J. Lan, E.-J. Ye, W.-Q. Sui, and X. Zhao, *Eur. Phys. J. B* **87**, 251 (2014).

[36] J. Dai and X. C. Zeng, *Angew. Chem.-Int. Ed.* **54**, 7572 (2015)

[37] Y. Jin, X. Li, and J. Yang, *Phys. Chem. Chem. Phys.* **17**, 18665 (2015).

[38] F. Iyikanat, R. T. Senger, F. M. Peeters, and H. Sahin, *Chem. Phys. Chem.* **17**, 3985 (2016).

[39] J. A. Silva-Guillen, E. Canadell, P. Ordejon, F. Guinea, and R. Roldan, *2D Mater.* **4**, 025085 (2017).

[40] E. Finkman and B. Fisher, *Solid State Commun.* **50**, 25 (1984).

[41] D. Pacilé, M. Papagno, M. Lavagnini, H. Berger, L. Degiorgi, and M. Grioni, *Phys. Rev. B* **76,** 155406 (2007).

[42] W. Schairer and M. W. Shafer, *Phys. Status Solidi* **17**, 181 (1973).

[43] P. A. Dowben, C. Binek, K. Zhang, L. Wang, W-N Mei, J. P. Bird, U. Singisetti, X. Hong, K. L. Wang, and D. Nikonov, *IEEE J. Explor. Solid State Comput. Dev. Circ*. **4**, 1 (2018).

[44] N. Sharma, C. Binek, A. Marshall, J. P. Bird, P. A. Dowben, and D. Nikonov, *31st IEEE Int. System-on-Chip Conf. (SOCC)* (Arlington, VA) IEEE Explore 146, (2018).

[45] D. E. Nikonov, C. Binek, X. Hong, J. P. Bird, K. L. Wang, and P. A. Dowben, US Patent 10361292B2 (2019).

[46] N. Sharma, J. P. Bird, C. Binek, P. A. Dowben, D. Nikonov, and A. Marshall, *Semicond. Sci. Technol.* **35**, 073001 (2020).

[47] Q. Zhao, Y. Guo, Y. Zhou, Z. Yao, Z. Ren, J. Bai, and X. Xu, *Nanoscale* **10,** 3547 (2018).

[48] M. Li, J. Dai, and X. C. Zeng *Nanoscale* **7**, 15385 (2015).

[49] H. Yi, S. J. Gilbert, A. Lipatov, A. Sinitskii, J. Avila, J. Abourahma, T. Komesu, M. C. Asensio, and P. A. Dowben, *J. Phys. Condens. Matter* **32**, 29LT01 (2020).

[50] W. Kong, C. Bacaksiz, B. Chen, K. Wu, M. Blei, X. Fan, Y. Shen, H. Sahin, D. Wright, D. S. Narang, and S. Tongay, *Nanoscale* **9**, 4175 (2017).

[51] A. Khatibi, R. H. Godiksen, S. B. Basuvalingam, D. Pellegrino, A. A. Bol, B. Shokri, and A. G. Curto, *2D Mater.* **7**, 015022 (2020).

[52] N. Papadopoulos, R. Frisenda, R. Biele, E. Flores, J. R. Ares, C. Sánchez, H. S. J. van der Zant, I. J. Ferrer, R. D'Agosta, and A. Castellanos-Gomez, *Nanoscale* **10**, 12424 (2018).

[53] E. Flores, J. R. Ares, I. J. Ferrer, and C. Sánchez, *Phys. Status Solidi - Rapid Res. Lett.* **10**, 802 (2016).

[54] K. Taniguchi, Y. Gu, Y. Katsua, Y. Takafumi, and H. Takagi, *Appl. Phys. Express* **9**, 011801 (2016).

[55] M. E. Fleet, S. L. Harmer, X. Liu, and H. W. Nesbitt, *Surf. Sci.* **584**, 133 (2005).

[56] A. S. Shkvarin, Y. M. Yarmoshenko, M. V. Yablonskikh, A. I. Merentsov, and A. N. Titov, *J. Struct. Chem.* **55**, 1039 (2014).

[57] J. G. Chen, *Surf. Sci. Rep*. **30**, 117 (1997).

[58] C. R. Dean, A. F. Young, I. Meric, C. Lee, L. Wang, S. Sorgenfrei, K. Watanabe, T. Taniguchi, P. Kim, K. L. Shepard, and J. Hone, *Nat. Nanotechnol.* **5**, 722 (2010).

[59] L. Wang, I. Meric, P. Y. Huang, Q. Gao, Y. Gao, H. Tran, T. Taniguchi, K. Watanabe, L. M. Campos, D. A. Muller, J. Guo, P. Kim, J. Hone, K. L. Shepard, and C. R. Dean, *Science* **342**, 614 (2013).

[60] S. Das, H.-Y. Chen, A. V. Penumatcha, and J. Appenzeller, *Nano Lett.* **13**, 100 (2013).

[61] Z. Zhang and J. T. Yates, *Chem. Rev.* **112**, 5520 (2012).

[62] R. I. Dzhioev, B. P. Zakharchenya, P. A. Ivanov, and V. L. Korenev, *JETP Lett.* **60**, 661 (1994).

[63] P. A. Dowben, D. E. Nikonov, A. Marshall, and C. Binek, *Appl. Phys. Lett.* **116**, 080502 (2020).

[64] P. A. Dowben, C. Binek, and D. E. Nikonov, *Nanoscale Silicon Devices*, ed. S Oda and D K Ferry (Boca Raton, FL: CRC Press) pp 255 (2016).

[65] R. Choudhary, P. Kumar, P. Manchanda, D. J. Sellmyer, P. A. Dowben, A. Kashyap, and R. Skomski, *IEEE Magn. Lett.* **7**, 3101604 (2016).

[66] S. Cao, Z. Xiao, C. P. Kwan, K. Zhang, J. P. Bird, L. Wang, W. N. Mei, X. Hong, and P. A. Dowben, *Appl. Phys. Lett.* **111**, 182402 (2017).

[67] S. C. Stuart, B. Gray, D. Nevola, L. Su, E. Sachet, M. Ulrich, and D. B. Dougherty, *Phys. Status Solidi - Rapid Res. Lett.* **10**, 242 (2016).

[68] M. Street, W. Echtenkamp, T. Komesu, S. Cao, P. A. Dowben, and C. Binek, *Appl. Phys. Lett.* **104**, 222402 (2014).

[69] N. Wu, X. He, A. L. Wysocki, U. Lanke, T. Komesu, K. D. Belashchenko, C. Binek, and P. A. Dowben, *Phys. Rev. Lett.* **106**, 087202 (2011).

[70] S. Cao, X. Xhang, N. Wu, A. T. N'Diaye, G. Chen, A. K. Schmid, X. Chem, W. Echtenkamp, A. Enders, C. Binek, and P. A. Dowben, *New J. Phys.* **16**, 073021 (2014).

[71] S. Cao, M. Street, J. Wang, J. Wang, X. Zhang, C. Binek, and P. A. Dowben *J. Phys.: Condens. Matter* **29**, 10LT01 (2017).

[72] X. He, Y. Wang, N. Wu, A. N. Caruso, E. Vescovo, K. D. Belashchenko, P. A. Dowben, and C. Binek, *Nat. Mater.* **9,** 579 (2010).

[73] C. Binek and B. Doudin, *J. Phys. Condens. Matter* **17**, L39 (2005).

[74] N. Sharma, J. P. Bird, P. A. Dowben, and A. Marshall *Semicond. Sci. Technol.* **31**, 065022 (2016).

[75] X. Chen, A. Hochstrat, P. Borisov, and W. Kleemann, *Appl. Phys. Lett.* **89**, 202508 (2006).

[76] M. Bibes and A. Barth´el´emy, *Nat. Mater.* **7**, 425 (2008).

2. Experimental Techniques

In this chapter, I will briefly describe the growth and characterization techniques used in this work with particular emphasis on photoemission spectroscopy.

2.1 Crystal Growth

TiS_3 crystals were grown by the Sinitskii group through the direct reaction of metallic titanium and sulfur vapor. In a typical synthesis, 0.1 g of a 0.25 mm thick Ti foil and 0.2 g of S are sealed in an evacuated (p 200 mTorr) quartz ampule furnace and annealed for 5 days at temperatures up to 550 °C. The ZrS_3 crystals were also grown through the direct reaction of elemental precursors. In a typical synthesis, we combined ~0.1 g of Zr foil and ~0.115 g (corresponding to ~10% molar excess in stoichiometry) of sulfur powder, sealed the mixture in a quartz ampoule under the pressure of ~ 200 mTorr and annealed it at 650 °C for two weeks.

The crystals of TiS_3 and ZrS_3 were characterized by x-ray diffraction (XRD) measurements in air at room temperature using a Rigaku Smart Lab diffractometer equipped with a Cu Kα source, λ = 1.5406 Å. Our XRD analysis indicates that the TiS_3 nanowhiskers conform to a monoclinic structure, with space group: $P2_1/m$, as illustrated in Figure 2.1, with TiS_3 lattice constants of a = 4.9728(6) Å, b = 3.4055(4) Å, c = 8.8146(15) Å and a cant angle of β = 97.56(1)°. These values remain in general agreement with earlier reported values of: a ranging from 4.849 to 4.973 Å, b from 3.326 to 3.433 Å, c from 8.714 to 8.815 Å, and β from 97.32 to 97.74◦ [1-6]. For ZrS_3, from XRD as shown in Figure 2.1(c), the lattice constants are slightly larger with a = 5.1107(4) Å, b = 3.6179(2) Å, c = 8.9725(5), and β = 97.64(1)◦ which are comparable to previously reported values for ZrS_3 ranging from 5.116 to 5.173 Å for a, 3.611 to 3.635 Å for b, 8.965 to 9.012 Å for c, and 97.13 to 97.46◦ for β [4,6-11].

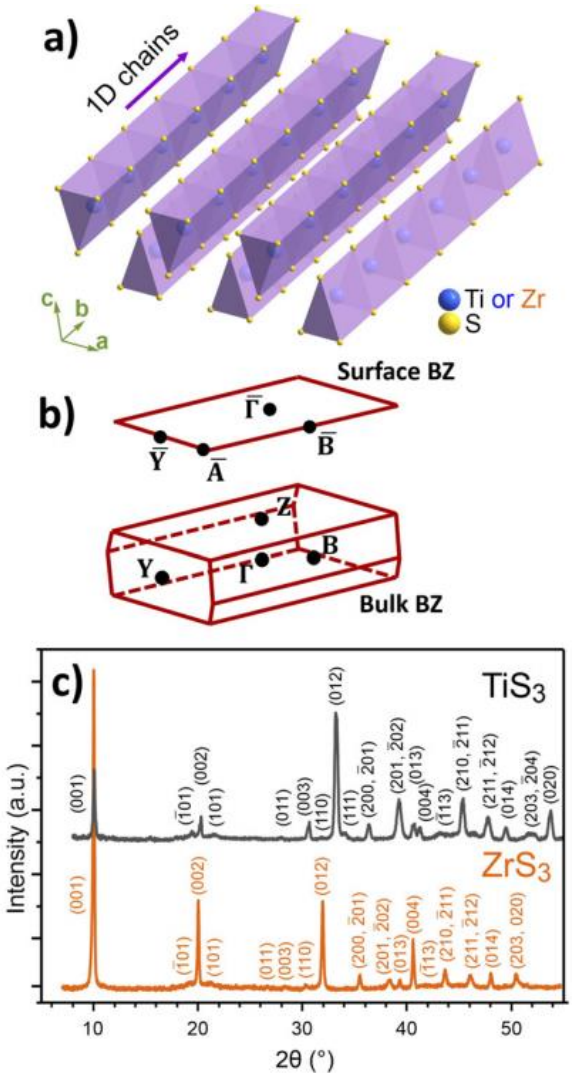

Figure 2.1 *(a) A schematic of the structure of a monolayer of TiS_3 or ZrS_3. (b) The surface and bulk Brillouin zones for TiS_3(001) or ZrS_3(001). (c) The XRD pattern taken from the TiS_3 and ZrS_3 powders. The XRD measurement and analysis was performed by Alexey Lipatov. Figure published in H. Yi, S. J. Gilbert, A. Lipatov, A. Sinitskii, J. Avila, J. Abourahma, T. Komesu, M. C. Asensio, and P. A. Dowben, J. Phys. Condens. Matter* ***32****, 29LT01 (2020).*

2.2 Photoemission Spectroscopy

Photoemission spectroscopy is a surface sensitive measurement technique which is based off of the photoelectric effect. In this measurement, a sample is placed into ultra-high vacuum (UHV) and then illuminated with a light source of known wavelength. The incident photons are absorbed by the electrons within the sample which are then emitted into the vacuum. By utilizing a hemispherical analyzer, the kinetic energy of the emitted electrons is measured and then used to determine the binding energies of the electrons within a sample based on equation 2.1 [12,13], where $h\nu$ is the energy of the incident photons, BE and KE are the binding and kinetic energies of the emitted electron, respectively, and φ is the work function of the sample.

$$h\nu = BE + KE + \varphi \tag{2.1}$$

In photoemission, the binding energy is defined as the energy difference between the bound electron state and the Fermi level (E_F), and φ is the energy difference between the Fermi level and the vacuum level. Because the samples are grounded, the Fermi level placement, and therefore φ, is constant for a given experimental setup, and can therefore be determined beforehand. The energy of the incident light can be altered to perform X-ray photoemission spectroscopy (XPS) or ultra-violet photoemission spectroscopy (UPS).

The XPS reported in Figures 5.2a and 5.2b was taken at the synchrotron SOLEIL using a photon energy of 350 eV and an MBS deflection analyzer, with an angular and energy resolution of ~0.2° and ~20 meV, respectively. The XPS found in Figures 5.2c, 5.2d, 6.1, and 6.3 was taken at the University of Nebraska-Lincoln with a SPECS XR50 X-ray source using non-monochromaized Al-Kα radiation ($h\nu$=1486.6 eV). Figures 5.2c, 6.1, and 6.3 used a VG100AX hemispherical electron analyzer while Figure 5.2d used a PHI Model 10-360 hemispherical electron analyzer.

In angle resolved photoemission spectroscopy (ARPES) [14] momentum conservation is used in addition to energy conservation so that the electron distribution can be plotted as a function of wave vector in addition to binding energy. This is accomplished using equations 2.2 and 2.3 where $k_{\parallel}$ and $k_{\perp}$ are the

$$KE = \frac{\hbar^2}{2m}\left(k_{||}^2 + k_{\perp}^2\right) \tag{2.2}$$

$$k_{||} = \sin(\theta)\sqrt{\frac{2m}{\hbar^2}KE} \tag{2.3}$$

components of the electron's momentum parallel and perpendicular the sample surface, respectively, m is the electron mass, and θ is the emission angle. Only the momentum parallel to the sample surface is conserved across the sample-vacuum interface so that the electron distribution is determined only for the surface Brillouin zone (BZ). The surface Brillouin zone for the transition metal trichalcogenides is illustrated in Figure 2.1b. All ARPES data was taken at the synchrotron SOLEIL using an MBS deflection analyzer.

2.3 Scanning Photocurrent Microscopy (SPCM)

In scanning photocurrent microscopy and laser is focused onto the channel of a phototransistor and the excited photocurrent is measured as a function of the laser position. In Chapter 4, SPCM was performed with a 488 nm solid state laser (Coherent Sapphire 100) passed through a neutral density filter followed by a linear polarizer before being reflected off a dichroic mirror and focused onto the phototransistors using an inverted Olympus IX 81 microscope. The neutral density filter was used to maintain a light intensity of 100 μW for all measurements. Measurements were performed at normal incidence, so that the incident light was polarized

perpendicular to the $\vec{c}$ axis. For more information on the SPCM setup see Li *et al.* [15] and Chen *et al.* [16].

2.4 X-ray Absorption Spectroscopy (XAS)

X-ray absorption spectroscopy (XAS) is similar to photoemission in that electrons within the sample absorb the energy of incident photons. However, in XAS the photon energy is tuned so that the electrons of interest are excited into the unoccupied conduction band states rather than being emitted into the vacuum. By directly or indirectly measuring the number of absorbed X-rays as a function of X-ray energy, the distribution of conduction band states can be measured [17-20]. There are generally 3 measurement modes of measuring XAS. Transmission mode directly measures the portion of X-rays that are absorbed by comparing the incident and transmitted X-ray intensities. The other detection modes are the fluorescence and electron yield modes which are indirect measurements and detect either photons or electrons, respectively, which are emitted as a result of secondary processes. The XAS measurements reported in Chapter 5 were measured at the synchrotron SOLEIL using the total electron yield, where the sample drain current was recorded by a floating nano-ampmeter. For more experimental details see [21].

2.5 Photoemission Electron Microscopy (PEEM)

When XAS is performed in the electron yield mode, it can be combined with photoemission electron microscopy (PEEM). The ejected Auger electrons, secondary electrons, and photoelectrons are passed through a variety of electron optics to provide a spatially resolved image of the ejected electron intensity distribution. By taking a series of images using different photon energies, a spatially resolved XAS spectra can be derived with typical resolutions on the micrometer scale.

2.6 X-ray Magnetic Circular Dichroism (XMCD)

A variation of XAS know as X-ray magnetic circular dichroism (XMCD) performs XAS measurements using circularly polarized light. Two XAS spectra are taken with either the sample magnetization or the circular light polarization switched, and the difference between the two spectra illuminates the spin polarization of the conduction band states [22-24]. In Chapter 7, XMCD was combined with PEEM at the SM beamline of the Canadian Light Source.

References

[1] J. O. Island, M. Barawi, R. Biele, A. Almazán, J. M. Clamagirand, J. R. Ares, C. Sánchez, H. S. J. Van Der Zant, J. V. Álvarez, R. D'Agosta, I. J. Ferrer, and A. Castellanos-Gomez, *Adv. Mater.* **27**, 2595 (2015).

[2] H. Yi, T. Komesu, S. Gilbert, G. Hao, A. J. Yost, A. Lipatov, A. Sinitskii, J. Avila, C. Chen, M. C. Asensio, and P. A. Dowben, *Appl. Phys. Lett.* **112**, 052102 (2018).

[3] S. J. Gilbert, A. Lipatov, A. J. Yost, M. J. Loes, A. Sinitskii, and P. A. Dowben, *Appl. Phys. Lett.* **114**, 101604 (2019).

[4] L. Brattås, A. Kjekshus, J. Krogh-Moe, J. Songstad, and Å. Pilotti *Acta Chem. Scand.* **26**, 3441 (1972).

[5] S. Kikkawa, M. Koizumi, S. Yamanaka, Y. Onuki, and S. Tanuma *Phys. Status Solidi A* **61**, K55 (1980).

[6] S. Furuseth, L. Brattås, and A. Kjekshus *Acta Chem. Scand. A* **29**, 623 (1975).

[7] A. Pant, E. Torun, B. Chen, S. Bhat, X. Fan, K. Wu, D. P. Wright, F. M. Peeters, E. Soignard, H. Sahin, and S. Tongay, *Nanoscale* **8**, 16259 (2016).

[8] Y. Jin, X. Li, and J. Yang, *Phys. Chem. Chem. Phys.* **17**, 18665 (2015).

[9] M. Li, J. Dai, and X. C. Zeng *Nanoscale* **7**, 15385 (2015).

[10] H. Jin, D. Cheng, J. Li, X. Cao, B. Li, X. Wang, X. Liu, and X. Zhao, *Solid State Sci.* **13**, 1166 (2011).

[11] L. Huang, K. Tang, Q. Yang, G. Shen, and S. Jia *Mater. Res. Bull.* **39**, 1083 (2004).

[12] A. J. Yost, P. E. Evans, I. Tanabe, G. Hao, S. Gilbert, and T. Komesu, *Integrated Experimental Methods for the Investigation of the Electronic Structure of Molecules on Surfaces*. In Springer Handbook for Surface Science; Springer, (2020).

[13] S. Hufner, *Photoelectron Spectroscopy* 3rd edn; Berlin: Springer, (2003).

[14] E. W. Plummer and W. Eberhardt, *Adv. Chem. Phys.* **49**, 533 (1982)

[15] M. Li, J-S Chen, P. K. Routh, P. Zahl, C-Y Nam, and M. Cotlet, *Adv. Funct. Mater.* **28**, 1707558 (2018).

[16] J. S. Chen, M. Li, Q. Wu, E. Fron, X. Tong, and M. Cotlet, *ACS Nano* **13**, 8461 (2019).

[17] C. S. Schnohr and M. C. Ridgway, 2015 *X-ray absorption spectroscopy of semiconductors*, Berlin: Springer (2015).

[18] C.N. Borca, T. Komesu, and P.A. Dowben, *J. Electron Spectros. Relat. Phenomena* **122**, 259 (2002).

[19] J. Stöhr *NEXAFS Spectroscopy*, Berlin: Springer (1992).

[20] J.C. Fuggle and J.E. Inglesfield, editors, *Unoccupied Electronic States*, Berlin, Heidelberg: Springer (1992).

[21] C. Chen, J. Avila, E. Frantzeskakis, A. Levy, and M.C. Asensio, *Nature Communications* **6**, 8585 (2015).

[22] N. Wu, X. He, A. L. Wysocki, U. Lanke, T. Komesu, K. D. Belashchenko, C. Binek, and P. A. Dowben *Phys. Rev. Lett.* **106**, 087202 (2011).

[23] S. Cao, M. Street, J. Wang, J. Wang, X. Zhang, C. Binek, and P. A. Dowben *J. Phys. Condens. Matter* **29**, 10LT01 (2017)

[24] C. T. Chen, Y. U. Idzerda, H. J. Lin, N. V. Smith, G. Meigs, E. Chaban, G. H. Ho, E. Pellegrin, and F. Sette *Phys. Rev. Lett.* **75**, 152 (1995).

3. The Valence Band Structure of TiS_3 and ZrS_3

The band structure of the occupied states of TiS_3(001) and ZrS_3(001) was experimentally determined using angle-resolved photoemission. Nanospot angle resolve photoemission spectroscopy (nanoARPES) was taken on TiS_3 and ZrS_3 crystals which were exfoliated *in situ* at a pressure of ~10^{-10} torr. The distances along the surface Brillouin zone, schematically shown in Figure 2.1b, for the surface Brillouin zone critical points from $\bar{\Gamma}$ to $\bar{B}$ and $\bar{\Gamma}$ to $\bar{Y}$, are determined by the lattice constants a and b. The corresponding distances in reciprocal space from $\bar{\Gamma}$ to $\bar{B}$ and $\bar{\Gamma}$ to $\bar{Y}$ for ZrS_3(001) are approximately 0.615 $Å^{-1}$ and 0.868 $Å^{-1}$, respectively, as indicated in Figure 3.1. This leads to a smaller surface Brillouin zone than is observed for TiS_3(001), 0.632 $Å^{-1}$ ($\bar{\Gamma}$ to $\bar{B}$) and 0.923 $Å^{-1}$ ($\bar{\Gamma}$ to $\bar{Y}$), which is also indicated in Figure 3.1. The nanoARPES is used to determine to position of the top of the BZ which provides information on the band gap as well as the majority carriers. The parabolas at the top of the valence band can be fit using the energy-momentum relation shown in equation 3.1 where E is the energy of the electron state, k is the wave vector, and m^* is the electron's effective mass.

$$E = \frac{\hbar^2 k^2}{2m^*} \tag{3.1}$$

3.1 The Valence Band Maximum

Figure 3.1 shows the nanoARPES spectra along the high symmetry directions of the surface Brillouin zone, from $\bar{\Gamma}$ to $\bar{Y}$ (parallel to the 1D chains) and from $\bar{\Gamma}$ to $\bar{B}$ (perpendicular to the chains), for both TiS_3(001) and ZrS_3(001), which are in general agreement with the calculated band structures [1-6]. The experimental electronic band structure is consistent with valence states of S 3p character, with only a limited admixture contribution of the Zr 4d states. In particular, the highest occupied states are derived from antibonding hybrid states of Π^*_g symmetry, with

contributions from the 3p states of the sulfur and the Zr 5p and 4d states, while the first empty states have an antibonding σ^*_u character, with an S 3p and Zr 4d and 5p character [1-6].

Along both high symmetry directions, in the experimental band structure of TiS_3(001) determined by angle resolved photoemission, the top of the valence band is dominated by a single band centered at the center of the surface Brillouin zone, $\bar{\Gamma}$, (Figures 3.1a-b and 3.2a-b). The top of the valence band in TiS_3 lies ∼1.0 eV below the Fermi level which is consistent with an n-type semiconductor [7-11] with a band gap of ∼1 eV [4,12-14]. The top of valence band in TiS_3 occurs at the center of the surface Brillouin zone, $\bar{\Gamma}$, in agreement with DFT calculations.

For ZrS_3(001), multiple bands can be seen near the top of the valence region, in the experimental band structure of ZrS_3(001), determined by angle resolved photoemission. Along the surface Brillouin zone line from $\bar{\Gamma}$ to $\bar{Y}$ (Figure 3.1c), two bands, centered at $\bar{\Gamma}$, can be seen at binding energies of ∼2–3 eV below the Fermi level. These bands have also been reported in a prior angle-resolved photoemission study of ZrS_3(001) [15]. In the $\bar{\Gamma}$ to $\bar{B}$ direction (Figure 3.1d), two bands, one centered at $\bar{\Gamma}$ and one centered between $\bar{\Gamma}$ to $\bar{B}$, can be seen at roughly 1.9 eV and 2.1 eV below the Fermi level, respectively. Given that ZrS_3(001) is expected to have a band gap of ∼1.8–2.1 eV [2-4,6,16-20], the placement of the top of the valence band ∼1.9 eV below the Fermi level is consistent with the strongly n-type character of ZrS_3 [19-22]. The two bands, observed at the top of the ZrS_3(001) valence band along $\bar{\Gamma}$ to $\bar{B}$, have been predicted by theory [2-6].

These experimental band structure measurements of ZrS_3(001) tend to indicate that the top of the valence band is at the center of the surface Brillouin zone, $\bar{\Gamma}$, which differs from the calculated band structure predictions [2-6], and the expectation that ZrS_3 is an indirect gap semiconductor [2-4,6,21,23]. Prior measurements have shown ZrS_3 to have an indirect optical band gap of ∼2 eV [21,23] and a direct optical band gap between 2.0 and 2.8 eV [17,21,23,24]. The bottom of the conduction band, in ZrS_3, is expected to occur at either the Γ [4-6] or Z [2,3] Brillouin

zone critical points. Meaning that if the valence band maximum actually occurs at $\bar{\Gamma}$, ZrS_3 could be a direct band gap semiconductor. Although, theoretical band structure calculations have predicted that the difference between the indirect and direct bandgaps becomes increasingly negligible as the size shrinks from bulk to monolayer [4]. Among the theoretical band structure calculations for ZrS_3(001) [2-6], the experimental band structure measurements shown here most closely resemble the calculated band structure for monolayer ZrS_3, under 2% biaxial tensile strain [6], in which the biaxial strain is predicted to result in an indirect to direct band gap transition. At this point, the situation might become better clarified with band structure calculations for both the surface and bulk of ZrS_3(001).

3.2 Anisotropic Carrier Mobility

As is evident in Figure 3.1, both TiS_3(001) (Figures 3.1a and b) and ZrS_3(001) (Figures 3.1c and d) show significant anisotropy along the surface Brillouin zone. This means that along the high symmetry lines of these trichalcogenides, the effective hole masses will differ. At the top of the valence band, the hole effective mass in TiS_3(001) is $-0.95 \pm 0.09m_e$ from $\bar{\Gamma}$ to $\bar{Y}$ and $-0.37 \pm 0.1m_e$ from $\bar{\Gamma}$ to $\bar{B}$. These values are close to the calculated effective hole masses of $-0.8333m_e$ [25] to $-0.98m_e$ [12] ($\bar{\Gamma}$ to $\bar{Y}$) and $-0.3317m_e$ [25] to $-0.32m_e$ [12] ($\bar{\Gamma}$ to $\bar{B}$). The measured hole effective mass for ZrS_3(001) is $-0.87 \pm 0.09m_e$ from $\bar{\Gamma}$ to $\bar{Y}$, slightly less than a previously reported value of $1.0m_e$ [15]. Along $\bar{\Gamma}$ to $\bar{B}$, for ZrS_3(001), the measured hole effective mass at the top of the valence band is $0.49 \pm 0.2m_e$. Figure 3 illustrates the fittings with these effective hole masses to experimental band structure at the top of the valence band for TiS_3(001) (Figures 3.2a and b) and ZrS_3(001) (Figures 3.2c and d). The ratio of the hole effective mass along $\bar{\Gamma}$ to $\bar{Y}$ vs $\bar{\Gamma}$ to $\bar{B}$ is 1.8:1 for ZrS_3(001), less than the hole effective mass ratio of 2.6:1 along the high symmetry directions for TiS_3(001), although the experimental uncertainties could significantly affect these ratios.

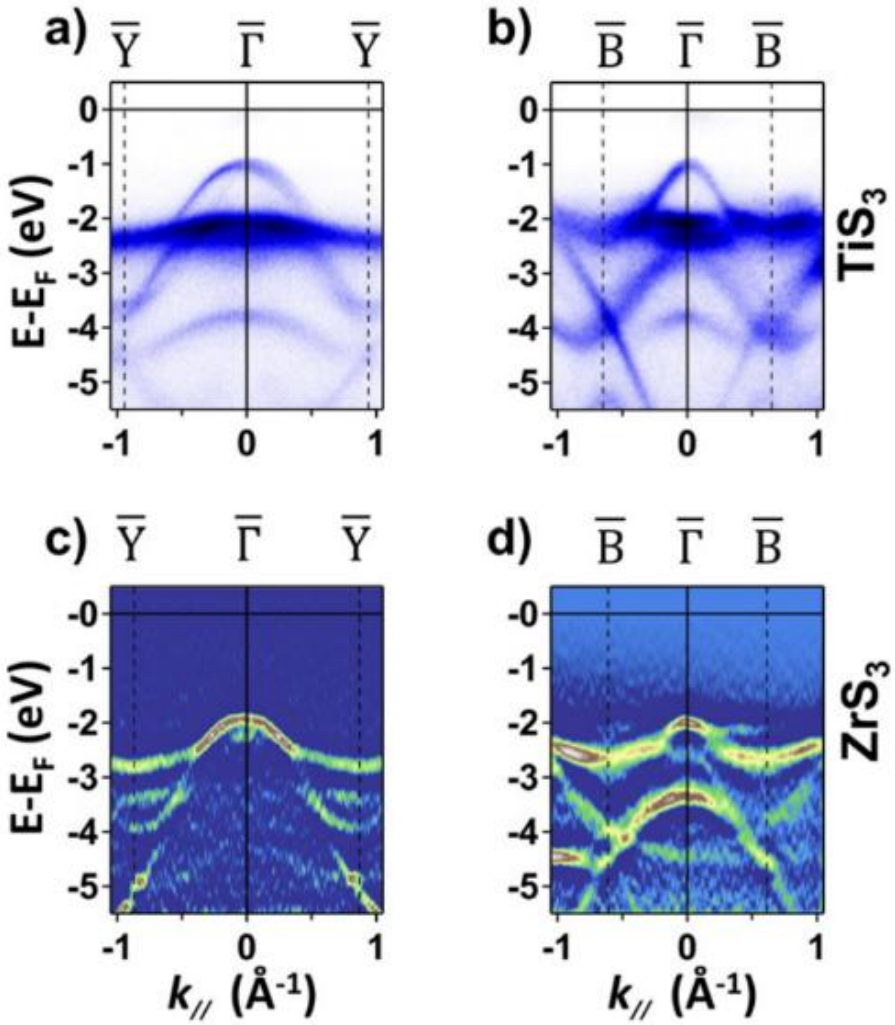

Figure 3.1 *The experimental band structure of TiS_3(001) [(a) and (b)] and ZrS_3(001) [(c) and (d)] along the high symmetry directions of $\overline{\Gamma}$ to $\overline{Y}$ [(a) and (c)] and $\overline{\Gamma}$ to $\overline{B}$ [(b) and (d)], as derived from nanoARPES. (c) and (d) are plots of the top of the valence band, after a taking the 2nd derivative of the experimental band structure, so as to illustrate the details of the band structure of ZrS_3(001). Measurements were taken by Hemian Yi. Figure published in H. Yi, S.J. Gilbert, A. Lipatov, A. Sinitskii, J. Avila, J. Abourahma, T. Komesu, M.C. Asensio, and P.A. Dowben, J. Phys.: Condens. Matter* ***32****, 29LT01 (2020).*

3.3 Summary

The band structure of the quasi-one-dimensional transition metal trichalcogenides TiS_3(001) and ZrS_3(001) were investigated using nanospot angle resolved photoemission spectroscopy and shown to have many similarities. We find that TiS_3 and ZrS_3 are both strongly n-type with the top of the valence band occurring at the center of the surface Brillouin zone. The band structure of both TiS_3 and ZrS_3 exhibit strong in-plane anisotropy, which results in a larger hole effective mass along the quasi-one-dimensional chains than perpendicular to them.

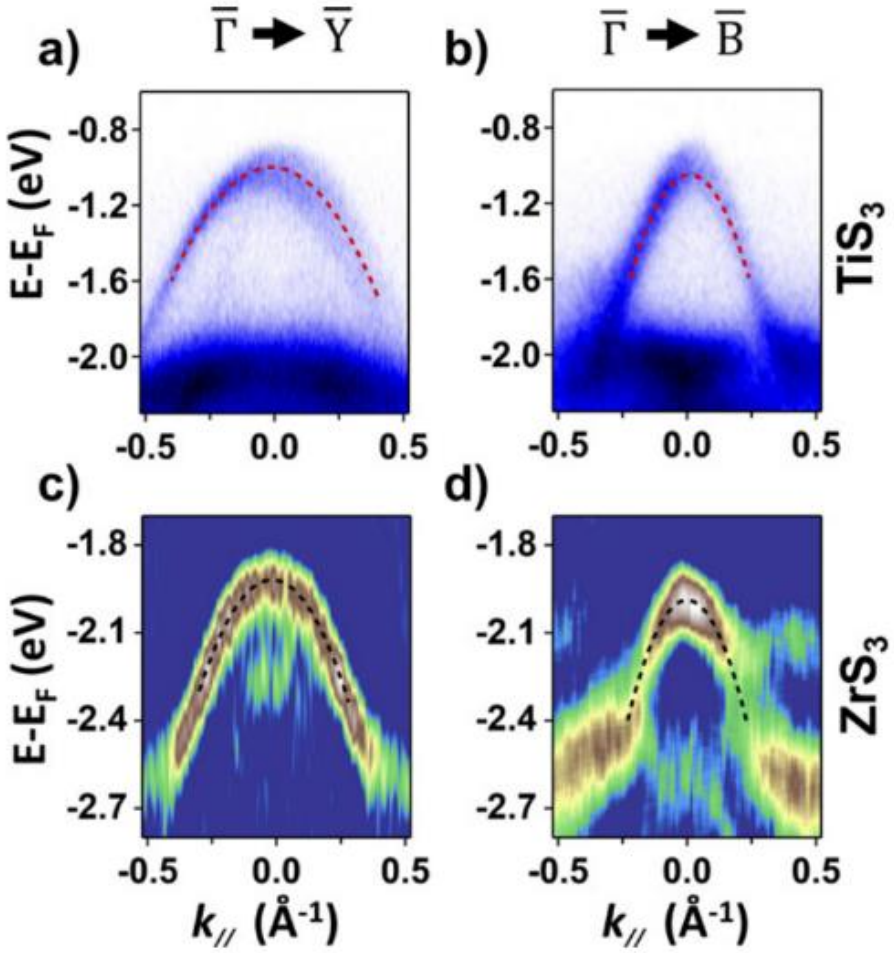

Figure 3.2 *The top of the valence band for TiS_3(001) [(a) and (b)] and ZrS_3(001) [(c) and (d)] along the high symmetry directions of $\overline{\Gamma}$ to $\overline{Y}$ [(a) and (c)] and $\overline{\Gamma}$ to $\overline{B}$ [(b) and (d)]. Dotted lines represent fitting curves used to calculate the effective hole masses of (a) $-0.95 \pm 0.09m_e$, (b) $-0.37 \pm 0.1m_e$, (c) -0.87 ± 0.09, and (d) $0.49 \pm 0.2m_e$. Data taken by Hemian Yi. Figure published in H. Yi, S.J. Gilbert, A. Lipatov, A. Sinitskii, J. Avila, J. Abourahma, T. Komesu, M.C. Asensio, and P.A. Dowben, J. Phys.: Condens. Matter* ***32****, 29LT01 (2020).*

References

[1] H. Yi, T. Komesu, S. Gilbert, G. Hao, A. J. Yost, A. Lipatov, A. Sinitskii, J. Avila, C. Chen, M. C. Asensio, and P. A. Dowben, *Appl. Phys. Lett.* **112**, 052102 (2018).

[2] A. Pant, E. Torun, B. Chen, S. Bhat, X. Fan, K. Wu, D. P. Wright, F. M. Peeters, E. Soignard, H. Sahin, and S. Tongay, *Nanoscale* **8**, 16259 (2016).

[3] X. Wang, K. Wu, M. Blei, Y. Wang L. Pan, K. Zhao, C. Shan, M. Lei, Y. Cui, B. Chen, D. Wright, W. Hu, S. Tongay, and Z. Wei, *Adv. Electron. Mater.* **5**, 1900419 (2019).

[4] Y. Jin, X. Li, and J. Yang, *Phys. Chem. Chem. Phys.* **17**, 18665 (2015).

[5] Q. Zhao, Y. Guo, Y. Zhou, Z. Yao, Z. Ren, J. Bai, and X. Xu, Nanoscale **10,** 3547 (2018)

[6] M. Li, J. Dai, and X. C. Zeng *Nanoscale* **7**, 15385 (2015).

[7] A. Lipatov, P. M. Wilson, M. Shekhirev, J. D. Teeter, R. Netusil, and A. Sinitskii, *Nanoscale* **7**, 12291 (2015).

[8] M. Randle, A. Lipatov, A. Kumar, C-P Kwan, J. Nathawat, B. Barut, S. Yin, K. He, N. Arabchigavkani, R. Dixit, T. Komesu, J. Avila, M. C. Asensio, P. A. Dowben, A. Sinitskii, U. Singisetti, and J. P. Bird, *ACS Nano* **13,** 803 (2018).

[9] J. O. Island, M. Barawi, R. Biele, A. Almazán, J. M. Clamagirand, J. R. Ares, C. Sánchez, H. S. J. Van Der Zant, J. V. Álvarez, R. D'Agosta, I. J. Ferrer, and A. Castellanos-Gomez, *Adv. Mater.* **27**, 2595 (2015).

[10] D. S. Muratov, V. O. Vanyushin, N. S. Vorobeva, P. Jukova, A. Lipatov, E. A. Kolesnikov, D. Karpenkov, D. V. Kuznetsov, and A. Sinitskii, *J. Alloys Compd.* **815**, 152316 (2020).

[11] J. Avila and M. C. Asensio, *Synchrotron Radiat. News* **27**, 24 (2014).

[12] J. Dai and X. C. Zeng, *Angew. Chem.-Int. Ed.* **54**, 7572 (2015).

[13] I. J. Ferrer, M. D. Maciá, V. Carcelén, J. R. Ares, and C. Sánchez, *Energy Procedia* **22**, 48 (2011).

[14] J. O. Island, M. Buscema, M. Barawi, J. M. Clamagirand, J. R. Ares, C. Sánchez, I. J. Ferrer, G. A. Steele, H. S. J. van der Zant, and A. Castellanos-Gomez, *Adv. Opt. Mater.* **2**, 641 (2014).

[15] D. Pacilé, M. Papagno, M. Lavagnini, H. Berger, L. Degiorgi, and M. Grioni, *Phys. Rev. B* **76,** 155406 (2007).

[16] L. Brattås, A. Kjekshus, J. Krogh-Moe, J. Songstad, and Å. Pilotti *Acta Chem. Scand.* **26**, 3441 (1972).

[17] S. Kurita, J. L. Staehli, M. Guzzi, and F. Levy, *Physica B* **105**, 169 (1981).

[18] G. Perluzzo, S. Jandl, and P. E. Girard, *Can. J. Phys.* **58**, 143 (1980).

[19] E. Flores, J. R. Ares, I. J. Ferrer, and C. Sánchez, *Phys. Status Solidi - Rapid Res. Lett.* **10**, 802 (2016).

[20] O. Gorochov, A. Katty, N. Le Nagard, C. Levy-Clement, A. Redon, and H. Tributsch, *J. Electrochem. Soc.* **130**, 1301 (1983).

[21] N. V. Morozova, I. V. Korobeinikov, K. V. Kurochka, A. N. Titov, and S. V. Ovsyannikov, *J. Phys. Chem. C* **122**, 14362 (2018).

[22] G. Perluzzo, A. A. Lakhani, S. and Jandl, *Solid State Commun.* **35**, 301 (1980).

[23] J. Avila, I. Razado, S. Lorcy, R. Fleurier, E. Pichonat, D. Vignaud, X. Wallart, and M. C. Asensio, *Sci. Rep.* **3**, 2439 (2013).

[24] W. Schairer and M. W. Shafer *Phys. Status Solidi* **17**, 181 (1973).

[25] J. A. Silva-Guillen, E. Canadell, P. Ordejon, F. Guinea, and R. Roldan, *2D Mater.* **4**, 025085 (2017).

4. The Effect of Band Symmetry on Photocurrent Production

In addition to their anisotropic electronic properties, which were discussed in the previous chapter, the transition metal trichalcogenides also possess strongly anisotropic optical properties, which are discussed in this chapter. Both scanning photocurrent microcopy (SPCM) and angle resolved photoemission spectroscopy (ARPES) measurements are extremely sensitive to the polarization of the exciting light. In SCPM microscopy, the photocurrent production is strongest when the light is polarized along the quasi-1D chain axis. By comparing these results to polarization dependent ARPES, we find that the photocurrent production is dominated by the S $3p_y$ orbitals, a conclusion which enables accurate predications regarding device performance.

4.1 Polarization Dependent SPCM on TiS_3(001) and ZrS_3(001)

The SPCM images of TiS_3 and ZrS_3 are shown in Figure 4.1 with an excitation energy of 2.5 eV (488 nm) and the incident light polarized along either the $\vec{b}$ (θ=0°) or $\vec{a}$ (θ=90°) axis. For both materials, the photocurrent intensity shows a notable polarization dependence which is consistent with other polarization studies on TiS_3(001) [1-5] and ZrS_3(001) [3,6,7]. However, the change in photocurrent intensity as a result of the changing light polarization is far more significant for ZrS_3(001) than for TiS_3(001), as seen by the photocurrent images in Figure 4.1, where the dichroic ratio for ZrS_3(001) is ~4:1, but for TiS_3(001) the ratio is only ~1.2:1. Photocurrent measurements, in previous studies, have shown dichroic ratios as high as 4:1 for TiS_3 [1] and 2.55:1 for ZrS_3 [6], and the dichroic ratio has been reported to depend on both the excitation energy [1,2,6] and sample thickness [3,6].

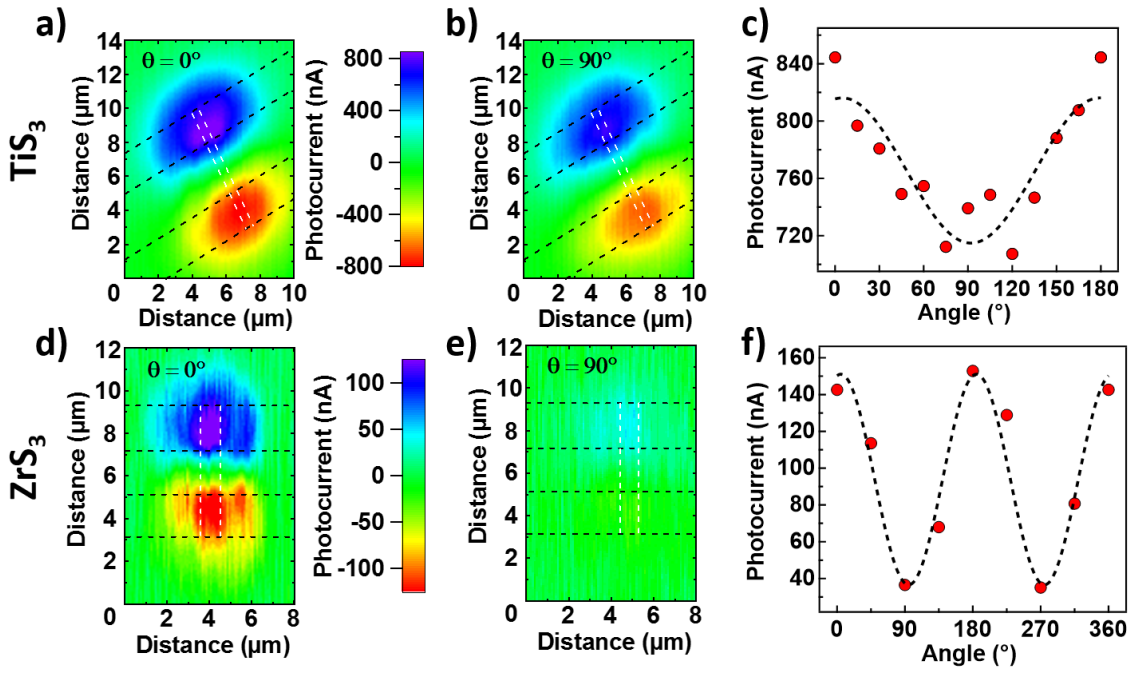

Figure 4.1 *Scanning photocurrent microscopy images of TiS_3(001) (a,b) and ZrS_3(001) (d,e) using light polarized along the $\vec{b}$ (a,d) and $\vec{a}$ (b,e) axis. The dotted black and white lines indicate the contacts and transistor channel respectively. The angle dependence of the photocurrent intensity in TiS_3(001) (c) and ZrS_3(001) (f) where the angle is measured with respect to the b-axis. The photocurrent intensities in c and f are the average of the photocurrent magnitudes at the source and drain. Figure published in S.J. Gilbert, H. Yi, J-S Chen, A.J. Yost, A. Dhingra, J. Abourahma, A. Lipatov, J. Avila, T. Komesu, A. Sinitskii, M.C. Asensio, and P.A. Dowben, "The Effect of Band Symmetry on Photocurrent Production in the Quasi-One-Dimensional Transition Metal Trichalcogenides," ACS Appl. Mater. Interfaces* **12**, 40525 (2020).

4.2 Selection Rules

The light polarization dependent photocurrent production can be explained by examining the average electron transition rate dictated by Fermi's golden rule [8-14] which is shown in Equation 4.1,

$$\Gamma = \frac{2\pi}{\hbar}\left|\langle\varphi_f|H'|\varphi_i\rangle\right|^2 \delta\left(E_f - E_i - \hbar\omega\right) \tag{4.1}$$

where φ_i, φ_f, E_i, and E_f are the initial and final state wave functions and energies, respectively, and H' is the perturbation Hamiltonian. For photoexcitation measurements, H' can be approximated as $\frac{e}{m_e c}\vec{A}\cdot\vec{P}$, where $\vec{A}$ is the vector potential and $\vec{P}$ is the momentum operator, under the assumptions that the field is sufficiently weak so that $\left|\vec{A}\right|^2$ is negligible and the momentum of the photon is negligible compared to the electron's momentum [13,14]. Using this approximation, $H'|\varphi_i\rangle$ is proportional to $\vec{\epsilon}\cdot\vec{r}$ where $\vec{\epsilon}$ is the light polarization vector and $\vec{r}$ is the dipole of the electron orbital. Furthermore, group theory considerations dictate that the transition will only occur if $\vec{\epsilon}\cdot\vec{r}$ belongs to the same irreducible representation as φ_f.

The transition metal trichalcogenides belong to the $P2_1/m$ space group [15-17], where the rotation axis is along the crystallographic $\vec{b}$ axis. This space group corresponds to the C_{2h} group symmetry in Schönflies notation. However, at the surface of the material both rotational and inversion symmetry are lost such that the group symmetry reduces to C_S. This loss of symmetry, and corresponding change in the selection rules, is likely responsible for the dependence of the dichroic ratio on sample thickness [3,6]. Based on density functional theory (DFT) calculations [18], the bottom of the conduction band in TiS_3 is dominated by the Ti $3d_{z^2}$ and $3d_{x^2-y^2}$ electron orbitals. Similarly, the bottom of the conduction in ZrS_3 should be largely Zr $4d_{z^2}$ and $4d_{x^2-y^2}$ [19]. All of these orbitals belong to the highest symmetry irreducible representations in the C_{2h} and

C_s symmetry groups. If the final states are limited to the d_{z^2} and $d_{x^2-y^2}$, then, in the bulk with C_{2h} symmetry, light polarized along the orbital y axis, (ϵ_y = along the chains) will exclusively excite electrons from the p_y orbitals, and light polarized along the x axis (ϵ_x) will excite the p_x orbitals. Due to the reduction of symmetry at the surface, ϵ_y can also excite the d_{yz} and d_{xy} orbitals, and $\epsilon_x + \epsilon_z$ can also excite the d_{xz}, d_{z^2}, and $d_{x^2-y^2}$ orbitals, though the latter two should have negligible contributions to the valence band [18,19]. These additional excitations will only occur if there is p-d hybridization since d→d transitions are optically forbidden [13-14]. The stronger photocurrent signal using ϵ_y (Figure 4.1) indicates that the p_y orbitals contribute most strongly to the photocurrent production.

4.3 Band Symmetries

The cause of the p_y dominance, in the dichroism of the photocurrent produciton, can be examined through symmetry assignments of the experimentally determined band structure using polarization dependent nanoARPES which is shown for TiS_3 and ZrS_3 in Figures 4.2 and 4.3, respectively. Photoemission is extremely surface sensitive with a final state that is a fully symmetric free electron such that the selection rules are the same as the photocurrent measurements. Electron orbitals within the same irreducible representations were distinguished with the assistance of previously reported DFT calculations [18,19].

Figure 4.2a schematically shows the light polarization geometry for the nanoARPES measurements on TiS_3(001) shown in Figure 4.2c where $\vec{\epsilon} = \epsilon_x + \epsilon_z$. The experimental band structure, illustrated in the figures in Chapter 3, utilized this polarization because this photoemission geometry emphasizes the top of the valence band, which may attributed to the S $3p_x$ orbitals [18,19]. These p_x orbitals are highly anisotropic with a hole effective mass that is twice as

large along $\bar{\Gamma}$ to $\bar{Y}$ than along $\bar{\Gamma}$ to $\bar{B}$, as noted earlier. The S $3p_z$ orbitals contribute most strongly to the band structure 2 eV below the Fermi level (E_F) or ~1 eV below the valence band maximum and these bands have minimal dispersion. The S $3p_z$ weighted bands are very evident with light polarized along $\epsilon_x + \epsilon_z$ (Figure 4.2c) and the symmetry selection rules allow photoemission from this initial state. The features of the S $3p_z$ bands can be more easily discerned after a 2nd derivative treatment of the data, which was reported in our previous work [16]. Both of these assignments are in agreement with DFT calculations [18].

When the light polarization is switched to $\vec{\epsilon} = \epsilon_z + \epsilon_y$ (Figure 4.2b) additional bands are observed near the top of the valence band (Figure 4.2d) which can be assigned to the S $3p_y$ orbitals. The S $3p_x$ and $3p_y$ orbital weighted bands at the top of the valence band are nearly degenerate at $\bar{\Gamma}$, the center of the surface Brillouin zone, contrary to DFT calculations, which place the $3p_y$ orbital weighted band at a binding energy well below the $3p_x$ orbital [1,7,18-20]. Unlike the $3p_x$ orbitals, the $3p_y$ bands have a significantly larger hole effective mass along the symmetry lines from $\bar{\Gamma}$ to $\bar{B}$ than along the lines from $\bar{\Gamma}$ to $\bar{Y}$. The $3p_x$ hybridized bands remain visible, though significantly weaker, with the light polarization perpendicular to the $\vec{x}$ orbital axis. This indicates that although these bands are mostly S $3p_x$ weighted, they also have other contributions which DFT calculations [18] place as largely the Ti $3d_{xz}$ orbitals.

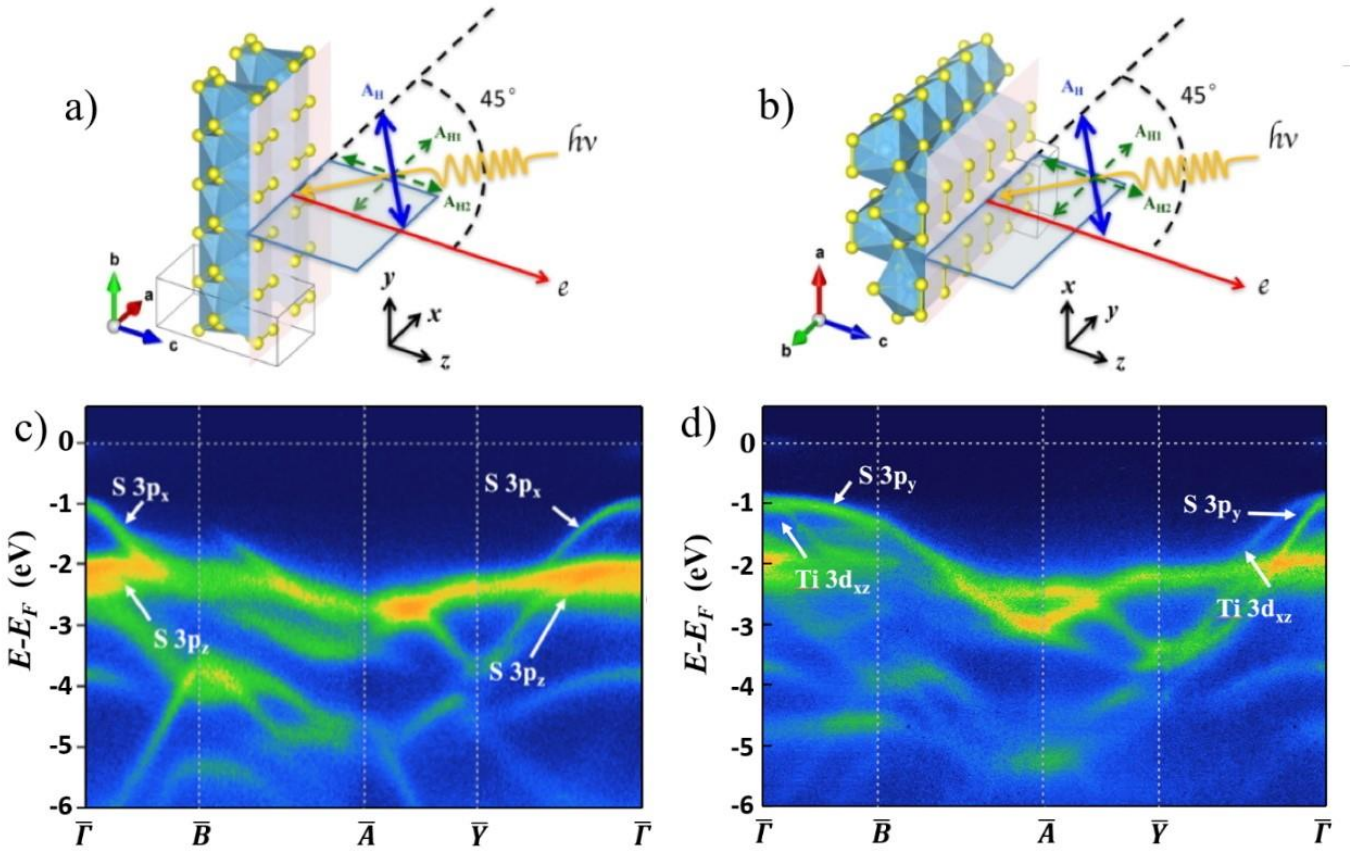

Figure 4.2 *The experimental setups illustrating polarization a)* $\epsilon_x + \epsilon_z$ *and b)* $\epsilon_z + \epsilon_y$ *used in the ARPES measurements of* TiS_3*(001) shown in c) and d), respectively. Taken at a photon energy of 100 eV. Data taken by Hemian Yi. Figure published in S.J. Gilbert, H. Yi, J-S Chen, A.J. Yost, A. Dhingra, J. Abourahma, A. Lipatov, J. Avila, T. Komesu, A. Sinitskii, M.C. Asensio, and P.A. Dowben, "The Effect of Band Symmetry on Photocurrent Production in the Quasi-One-Dimensional Transition Metal Trichalcogenides," ACS Appl. Mater. Interfaces* **12**, 40525 (2020).

The nanoARPES measurements, on ZrS_3(001), with polarization vectors ϵ_x, ϵ_y, and $\epsilon_x + \epsilon_z$ are shown in Figures 4.3a, 4.3b, and 4.3c respectively. As with TiS_3(001), the S $3p_x$ and $3p_y$ orbitals in ZrS_3(001) are both present near the top of the valence band and nearly degenerate at $\bar{\Gamma}$. Previous ARPES measurements on ZrS_3 attributed these two bands to spin-orbit coupling [21]. However, the orbital symmetries of these two bands are observed to be significantly different in Figure 4.3. Furthermore, the spectral weight assignments to sulfur weight p bands, as suggested by theory, and the absence of wave vector displacement that is typical of spin-orbit coupling, indicates that this band splitting at the top of the valence band at $\bar{\Gamma}$ is not dominated by spin-orbit splitting, and has no exchange splitting contribution.

The S $3p_x$ orbital is almost entirely absent in both Figures 4.3b and 4.3c which is consistent with S $3p_x$ with a minor Zr $4d_{xz}$ component dominating the top of the valence band. As with TiS_3, the S $3p_z$ character states in ZrS_3 contribute to the valence band structure at binding energies ~1 eV below the valence band maximum. These symmetry assignments are the same as seen in Figure 4.2 for TiS_3 and agree with DFT for TiS_3 [18] and ZrS_3 [19].

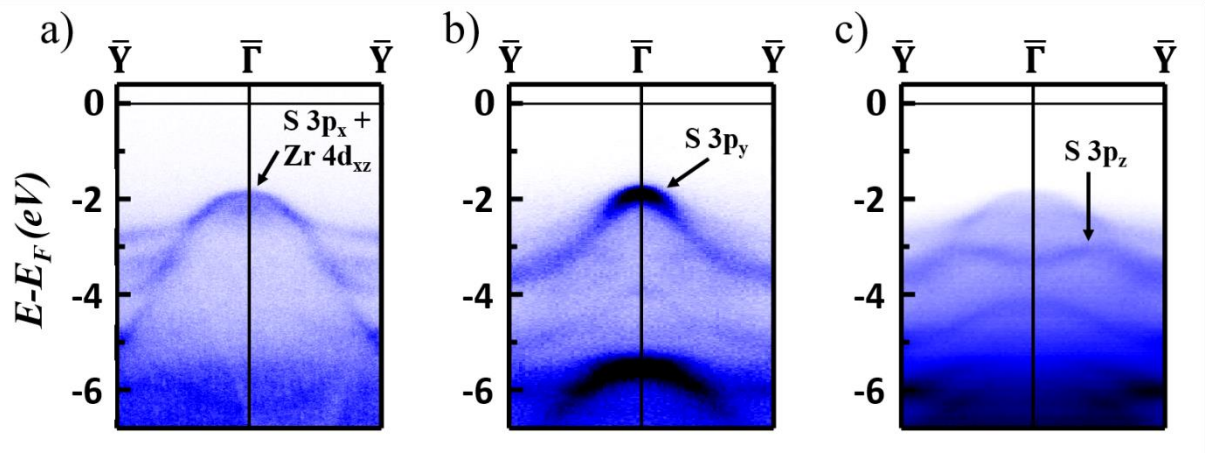

Figure 4.3 *The angle-resolved photoemission derived band structure of ZrS_3(001) using incident light polarizations a) ϵ_x, b) ϵ_y, and c) $\epsilon_x + \epsilon_z$. The photon energy is 130 eV. Data taken by Hemian Yi. Figure published in S.J. Gilbert, H. Yi, J-S Chen, A.J. Yost, A. Dhingra, J. Abourahma, A. Lipatov, J. Avila, T. Komesu, A. Sinitskii, M.C. Asensio, and P.A. Dowben, "The Effect of Band Symmetry on Photocurrent Production in the Quasi-One-Dimensional Transition Metal Trichalcogenides," ACS Appl. Mater. Interfaces* **12**, 40525 (2020).

Based on Figures 4.2 and 4.3, the S p_y orbitals extend from close to the valence band maximum to binding energies ~2 eV below the valence band maximum. The S p_y orbitals, nonetheless, have strong spectral weight density within 0.5 eV of the valence band maximum. Because the top of the valence band occurs at the center of the Brillouin zone [15,16], the near degeneracy of the p_y and p_x bands at the center of the Brillouin zone, $\bar{\Gamma}$, affects light polarization sensitivity. If the trichalcogenide S p_x orbitals occurred at significantly higher binding energies than the S p_y orbitals, as suggested by theory [1,7,18-20], then excitation energies close to the band gap would generate larger photocurrents with light polarized perpendicular to the 1D chains resulting in an region of photon energy where the dichroic ratio could switch.

Larger Z value transition metal trichalcogenides, specifically $ZrSe_3$ and $HfSe_3$, do exhibit an appreciable splitting, in binding energy, between the trichalcogenide S p_x and S p_y bands at $\bar{\Gamma}$ [21], but this splitting is not resolved here at $\bar{\Gamma}$, the center of the surface Brillouin zone, for TiS_3(001) and ZrS_3(001), as seen in Figures 4.2 and 4.3 respectively. Yet the existing band structure calculations [18,19], that include symmetry assignments, are seen to be in agreement with experiment. The band structure is also seen to be consistent with many of the device characteristics as noted elsewhere [22].

4.4 Summary

Since the d_{z^2} and $d_{x^2-y^2}$ orbitals dominate the bottom 0.5 eV of the conduction band for both ZrS_3 and TiS_3 [18,19], it is expected that the dichroic ratios will be maximized with excitation energies within 1 eV of the band gap and will begin to diminish for larger excitation energies. The band gaps for TiS_3 and ZrS_3 are ~1 eV [16,20,23-27] and ~2 eV [6,7,15,19,20,28-31], respectively, so that the dichroic ratios should be maximized with excitation energies of 1.0 to 2.0 eV for TiS_3 and 2.0 to 3.0 eV for ZrS_3. This conclusion is supported by comparison of the presently reported SPCM data with other experimental measurements [1-3,6]. Here the polarization dependence of the photoconductance is far more significant for ZrS_3(001) that for TiS_3(001), but the photon energy of 2.5 eV (488 nm) used here is much closer to the band gap of ZrS_3 than TiS_3. For TiS_3, the dichroic ratio has been observed to increase as the photon excitation energy is decreased from 2.3 eV to 1.5 eV [1]. Although the prior absorption calculations vary significantly [1,2,6,32], they tend to place the maximum dichroic ratio at slightly higher excitation energies which is likely caused by the discrepancies between calculated [1,7,18-20] and experimental [15,16,21] band structures mentioned earlier. Indeed, the optical excitation wavelength used here (488 nm) is very close to the observed optical resonance seen for ZrS_3 [33]. Despite possible discrepancies, it is clear that when combined TiS_3 and ZrS_3 have promise as polarization sensitive photodetectors over a wide range of wavelengths.

References

[1] S. Liu, W. Xiao, M. Zhong, L. Pan, X. Wang, H-X Deng, J. Liu, J. Li, and Z. Wei, *Nanotechnology* **29**, 184002 (2018).

[2] J. O. Island, R. Biele, M. Barawi, J. M. Clamagirand, J. R. Ares, C. Sánchez, H. S. J. Van Der Zant, I. J. Ferrer, R. D'Agosta, and A. Castellanos-Gomez, *Sci. Rep.* **6**, 22214 (2016).

[3] W. Kong, C. Bacaksiz, B. Chen, K. Wu, M. Blei, X. Fan, Y. Shen, H. Sahin, D. Wright, D. S. Narang, and S. Tongay, *Nanoscale* **9**, 4175 (2017).

[4] A. Khatibi, R. H. Godiksen, S. B. Basuvalingam, D. Pellegrino, A. A. Bol, B. Shokri, and A. G. Curto, *2D Mater.* **7**, 015022 (2020).

[5] N. Papadopoulos, R. Frisenda, R. Biele, E. Flores, J. R. Ares, C. Sánchez, H. S. J. van der Zant, I. J. Ferrer, R. D'Agosta, and A. Castellanos-Gomez, *Nanoscale* **10**, 12424 (2018).

[6] X. Wang, K. Wu, M. Blei, Y. Wang L. Pan, K. Zhao, C. Shan, M. Lei, Y. Cui, B. Chen, D. Wright, W. Hu, S. Tongay, and Z. Wei, *Adv. Electron. Mater.* **5**, 1900419 (2019).

[7] A. Pant, E. Torun, B. Chen, S. Bhat, X. Fan, K. Wu, D. P. Wright, F. M. Peeters, E. Soignard, H. Sahin, and S. Tongay, *Nanoscale* **8**, 16259 (2016).

[8] P. J. Feibelman, and D. E. Eastman, *Phys. Rev. B* **10**, 4932 (1974).

[9] G. D. Mahan, *Phys. Rev. B* **2**, 4334 (1970).

[10] I. Adawi, *Phys. Rev.* **134**, A788 (1964).

[11] W. L. Schaich, and N. W. Ashcroft, *Phys. Rev. B* **3**, 2452 (1971).

[12] M. C. Asensio, J. Avila, L. Roca, A. Tejeda, G. D. Gu, M. Lindroos, R. S. Markiewicz, and A. Bansil, *Physical Review B* **67**, 014519 (2003).

[13] P.A. Dowben, J. Choi, E. Morikawa, and B. Xu, *The Band Structure and Orientation of Molecular Adsorbates on Surfaces by Angle-Resolved Electron Spectroscopies*, in: Handbook of Thin Films, edited by H.S. Nalwa, Volume 2: Characterization and Spectroscopy of Thin Films, Chapter 2 (Academic Press) pp. 61-114 (2002).

[14] E. W. Plummer and W. Eberhardt, *Adv. Chem. Phys.* **49**, 533 (1982)

[15] H. Yi, S. J. Gilbert, A. Lipatov, A. Sinitskii, J. Avila, J. Abourahma, T. Komesu, M. C. Asensio, and P. A. Dowben, *J. Phys. Condens. Matter* **32**, 29LT01 (2020).

[16] H. Yi, T. Komesu, S. Gilbert, G. Hao, A. J. Yost, A. Lipatov, A. Sinitskii, J. Avila, C. Chen, M. C. Asensio, and P. A. Dowben, *Appl. Phys. Lett.* **112**, 052102 (2018).

[17] S. Furuseth, L. Brattås, and A. Kjekshus *Acta Chem. Scand. A* **29**, 623 (1975).

[18] J. A. Silva-Guillen, E. Canadell, P. Ordejon, F. Guinea, and R. Roldan, *2D Mater.* **4**, 025085 (2017).

[19] M. Li, J. Dai, and X. C. Zeng *Nanoscale* **7**, 15385 (2015).

[20] Y. Jin, X. Li, and J. Yang, *Phys. Chem. Chem. Phys.* **17**, 18665 (2015).

[21] D. Pacilé, M. Papagno, M. Lavagnini, H. Berger, L. Degiorgi, and M. Grioni, *Phys. Rev. B* **76,** 155406 (2007).

[22] M. Randle, A. Lipatov, A. Kumar, C-P Kwan, J. Nathawat, B. Barut, S. Yin, K. He, N. Arabchigavkani, R. Dixit, T. Komesu, J. Avila, M. C. Asensio, P. A. Dowben, A. Sinitskii, U. Singisetti, and J. P. Bird, *ACS Nano* **13,** 803 (2018).

[23] J. O. Island, M. Buscema, M. Barawi, J. M. Clamagirand, J. R. Ares, C. Sánchez, I. J. Ferrer, G. A. Steele, H. S. J. van der Zant, and A. Castellanos-Gomez, *Adv. Opt. Mater.* **2**, 641 (2014).

[24] I. J. Ferrer, M. D. Maciá, V. Carcelén, J. R. Ares, and C. Sánchez, *Energy Procedia* **22**, 48 (2011).

[25] I. J. Ferrer, J. R. Ares, J. M. Clamagirand, M. Barawi, and C. Sánchez, *Thin Solid Films* **535**, 398 (2013).

[26] J. Dai and X. C. Zeng, *Angew. Chem.-Int. Ed.* **54**, 7572 (2015)

[27] A. J. Molina-Mendoza, M. Barawi, R. Biele, E. Flores, J. R. Ares, C. Sánchez, G. Rubio-Bollinger, N. Agraït, R. D'Agosta, I. J. Ferrer, and A. Castellanos-Gomez, *Adv. Electron. Mater.* **1**, 1500126 (2015).

[28] S. Kurita, J. L. Staehli, M. Guzzi, and F. Levy, *Physica B* **105**, 169 (1981).

[29] G. Perluzzo, S. Jandl, and P. E. Girard, *Can. J. Phys.* **58**, 143 (1980).

[30] E. Flores, J. R. Ares, I. J. Ferrer, and C. Sánchez, *Phys. Status Solidi - Rapid Res. Lett.* **10**, 802 (2016).

[31] O. Gorochov, A. Katty, N. Le Nagard, C. Levy-Clement, A. Redon, and H. Tributsch, *J. Electrochem. Soc.* **130**, 1301 (1983).

[32] E. Torun, H. Sahin, A. Chaves, L. Wirtz, and F. M. Peeters, *Phys. Rev. B* **98**, 075419 (2018).

[33] S. J. Gilbert, H. Yi, J-S Chen, A. J. Yost, A. Dhingra, J. Abourahma, A. Lipatov, J. Avila, T. Komesu, A. Sinitskii, M. C. Asensio, and P. A. Dowben, "The Effect of Band Symmetry on Photocurrent Production in the Quasi-One-Dimensional Transition Metal Trichalcogenides," *ACS Appl. Mater. Interfaces* **12**, 40525 (2020).

5. Strong Metal to Sulfur Hybridization

It was discussed in Section 4.3 that the top of the valence band in both TiS_3 and ZrS_3 is comprised of metal-sulfur hybridized bands. Here it is shown that there is also strong metal-sulfur hybridization in the conduction bands of these materials by comparing X-ray photoemission spectroscopy and X-ray absorption spectroscopy. The obtained X-ray absorption spectra are characterized by one or more transitions (absorption edges), where the photon energy position is element specific, since this coincides with the energy of the corresponding atomic core level. The X-ray transitions are typically controlled by the dipolar selection rules relating the well-defined atomic symmetry of the involved core hole and the final state angular momenta. In general, although very challenging for semiconductors and dielectrics, due to the potential for sample charging issues, the X-ray photoemission binding energies, with respect to the Fermi level, set the position of the conduction band minimum in the same core edge data in X-ray absorption, i.e. absent any charge, the photon energy in XAS, minus the core level binding energies sets the placement of the conduction band minimum and states above E_F, at a particular core edge.

5.1 XAS of TiS_3 and ZrS_3

The X-ray absorption spectra (XAS) taken at the 2*p* core level edges of Ti and S, for TiS_3, and the 2*p* edges of S and 3p edges of Zr, for ZrS_3, are shown in Figure 5.1. The Ti $2p_{3/2}$ and Ti $2p_{1/2}$ absorption edges differ by roughly 6.0 eV (Figure 5.1a), and the Zr $3p_{3/2}$ and Zr $3p_{1/2}$ edges, absorption edges differ by about 13.6 eV, as seen in Figure 5.1b. These separations are consistent with the binding energy shift as is observed in core level X-ray photoemission shown in Figures 5.2b and 5.2d. The two features seen near photon energies of 348 and 352 eV in Figure 5.1b are most likely attributed to $CaCo_3$ present in the epoxy used to mount the samples and resemble previous XAS measurements on the Ca 2*p* core level edges [1]. The Ca 2*p* photoelectron peaks are also seen in the XPS spectra shown in Figure 5.2d

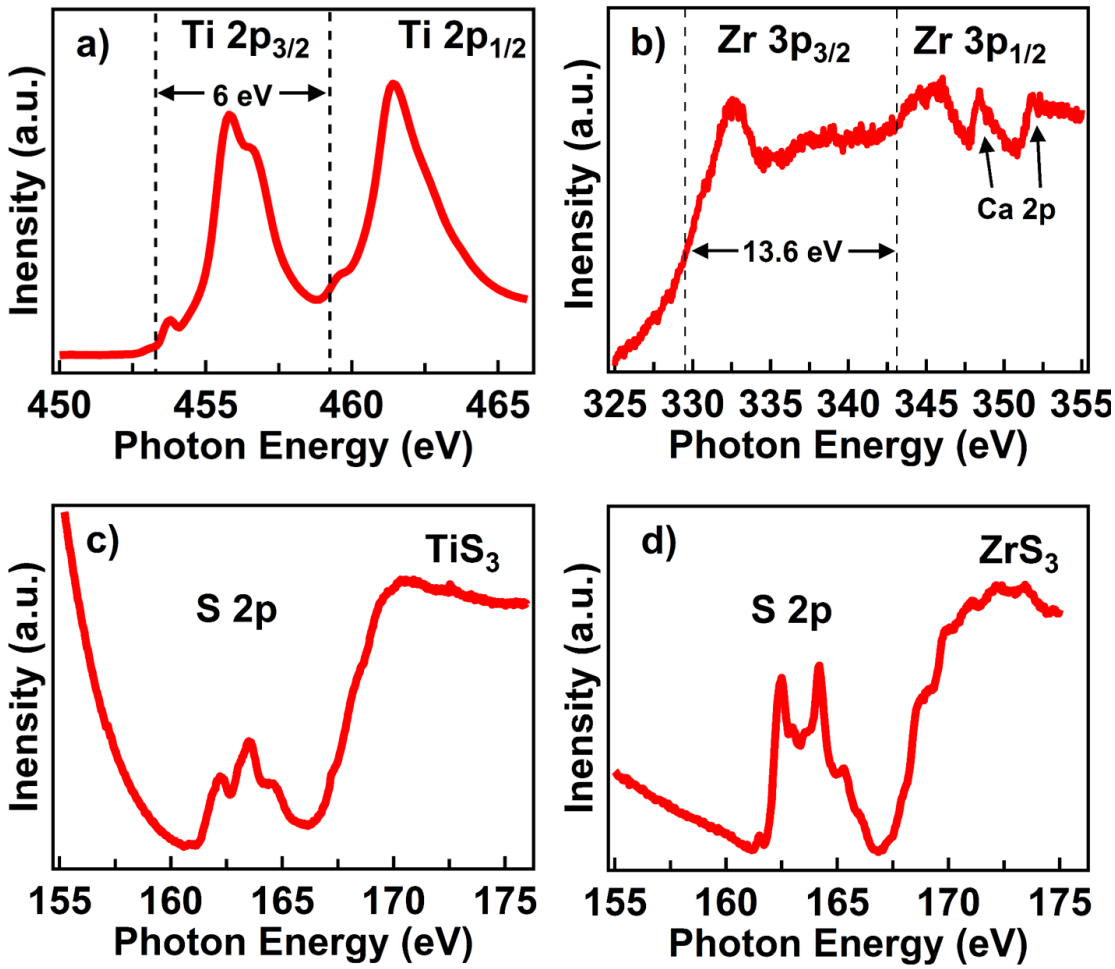

Figure 5.1 *The X-ray absorption spectra taken at (a) the Ti 2p edges for TiS_3, b) the Zr 3p edges for ZrS_3, c) the S 2p edges for TiS_3, and d) the S 2p edges for ZrS_3. Here the data is plotted as a function of incident photon energy. In b) the indicated Ca 2p threshold peaks are likely from $CaCo_3$ which is present in the epoxy used to mount the sample. Data taken by Hemian Yi. Figure submitted for publication in S.J. Gilbert, H. Yi, A. Lipatov, A.J. Yost, T. Komesu, A. Sinitskii, J. Avila, M.C. Asensio, and P.A. Dowben, "Strong Metal-Sulfur Hybridization in the Conduction Band of the Quasi-One-Dimensional Transition Metal Trichalcogenides: TiS_3 and ZrS_3," Submitted to J. Phys. Chem. C*

5.2 XPS of TiS_3 and ZrS_3

The core level XPS spectra shown in Figure 5.2 indicate the binding energies for the Ti 2p, S 2p, and Zr 3p core levels. These core levels are relevant to the XAS excitations shown in Figure 5.1 as they determine the absorption thresholds in XAS. The S 2p XPS spectra for TiS_3 and ZrS_3 both show triplet like features with peaks at 161.1 eV, 162.3 eV, and 163.5 eV for TiS_3 and at 161.5 eV, 162.7 eV, and 163.8 eV for ZrS_3. In TiS_3, the Ti $2p_{3/2}$ and $2p_{1/2}$ core level binding energies are 455.9 eV and 461.9 eV, respectively; and for the ZrS_3, the Zr $3p_{3/2}$ and $3p_{1/2}$ binding energies are 332.1 eV and 345.7 eV. These values are consistent with previous XPS measurements on TiS_3 [2-6] and ZrS_3 [7,8]. A slight variance of ~1-2 eV between the observed XPS binding energies and the photon energies at the XAS edges is due to uncertainty in the XAS photon energies due to monochromator drift. However, both TiS_3 [2,3,9-14] and ZrS_3 [9,14] are strongly n-type materials, as noted above, with the distance from the valence band to the Fermi level approximately equal to the band gap [3,15]. Thus, in order to place the XAS spectra in the context of the unoccupied states, the Fermi level has been placed at the leading edge of the X-ray absorption envelope grouping of features for each elemental core level studied here.

5.3 The Conduction Band of TiS_3

The observed absorption features for the Ti $2p_{3/2}$ and $2p_{1/2}$ states in TiS_3 are shown in Figures 5.3a and 5.3b, respectively, and are similar to previous studies [4,5]. The Ti $2p_{3/2}$ and $2p_{1/2}$ absorption spectra were both fit with 4 peaks. The $2p_{3/2}$ X-ray absorption spectra shows features located near 0.5, 1.8, 2.5 and 3.5 eV above the Fermi level, labeled A-D respectively, when corrected for the core level binding energies. In the $2p_{1/2}$ absorption edge X-ray spectra, peaks were found at 0.3, 1.5, 2.3 and 3.7 eV above the Fermi level, labeled E-H, when suitably corrected for the core level binding energies.

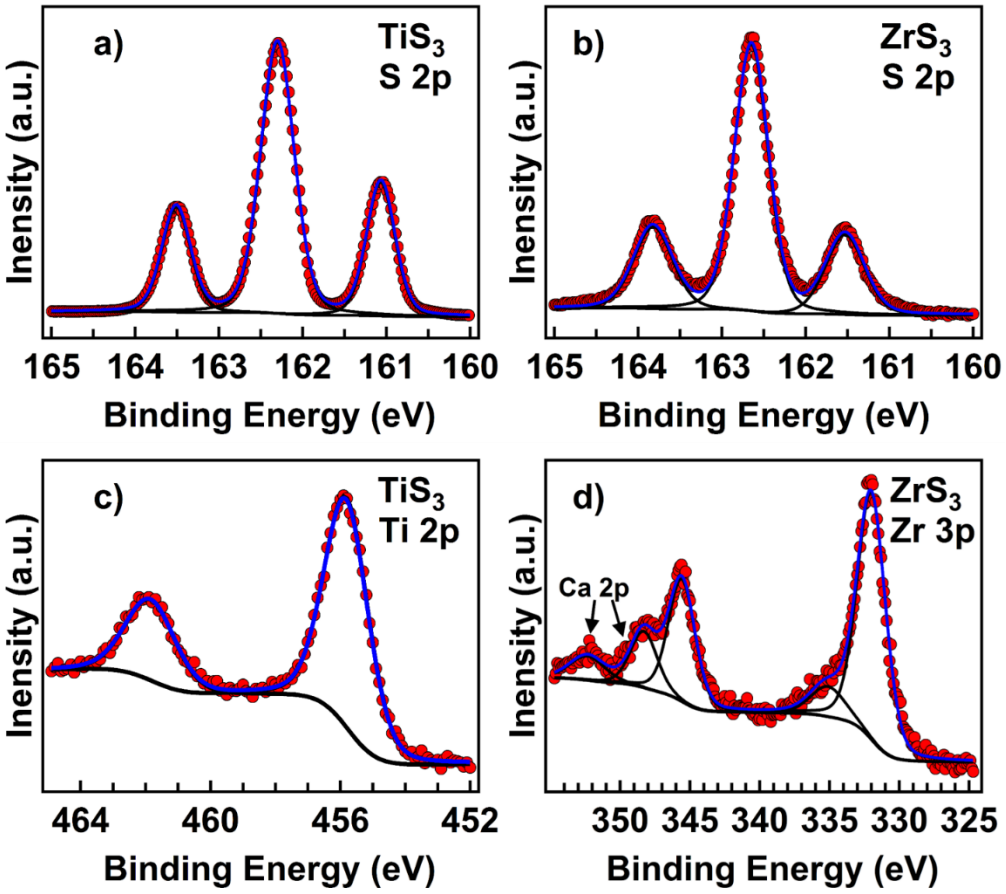

Figure 5.2 *The X-ray photoemission spectra for the following core level states: a) S 2p in TiS_3, b) S 2p in ZrS_3, c) Ti 2p in TiS_3, and d) Zr 3p in ZrS_3. Data in a) and b) was taken by Hemian Yi. Figure submitted for publication in S.J. Gilbert, H. Yi, A. Lipatov, A.J. Yost, T. Komesu, A. Sinitskii, J. Avila, M.C. Asensio, and P.A. Dowben, "Strong Metal-Sulfur Hybridization in the Conduction Band of the Quasi-One-Dimensional Transition Metal Trichalcogenides: TiS_3 and ZrS_3," Submitted to J. Phys. Chem. C*

The XAS spectra taken at the sulfur 2*p* core (Figure 5.3c), for TiS_3, is complicated by the proximity of the $2p_{1/2}$ and $2p_{3/2}$ core levels, which overlap in binding energy, and the presence of two non-equivalent sulfur sites in TiS_3 [2-6]. This gives rise to 3 separate core level components (due to the overlap of two peaks) for the sulfur 2*p* electrons in TiS_3, which are separated by a spin-orbit splitting of approximately 1.2 eV, as seen in the core level X-ray photoemission of Figure 5.2a. The placement of the Fermi level, as indicated in Figure 5.3c, corresponds to the transition from the lowest binding energy S 2*p* core level state to the conduction band minimum. Although the XAS spectra for the S 2*p* edge was fit with 6 peaks, these features are assigned to transitions from the three separate S 2*p* core level components, that occur at different binding energies. Of interest here are the transitions from the S 2*p* core level with the smallest binding energies to two low lying unoccupied states in the conduction band at approximately 1.3 and 1.8 eV above the Fermi level. A minor X-ray absorption feature, corresponding to a binding energy of around 0.3 eV above the Fermi level, is also seen in the inset of Figure 5.3c but was not considered in the fitting. The very low intensity of the S core edge XAS features, corresponding to unoccupied states within 1 eV above the relative Fermi level, indicates that the bottom of the conduction band is not strongly sulfur weighted in TiS_3. This is consistent with our theoretical expectations. As seen in Figure 5.4, the expectation is that the bottom of the conduction band is Ti 3*d*, with negligible S weight.

The two allowed transitions for the Ti 2p XAS spectra are $p \rightarrow s$ and $p \rightarrow d$. However, it has been argued that the $2p \rightarrow s$ contributions to the XAS spectra tend to be smaller for strongly ionic 3*d* compounds [4,16]. The assignment of the observed transitions to *d* final states is further supported by the XAS spectra taken at the threshold of the spin-orbit split Ti 2*p* core, as plotted in Figures 5.3a and 5.3b. While some theoretical calculations, nonetheless, predict that the Ti *s* states will be dominant at the conduction band minimum [17], as just noted, our theoretical predictions indicate that the bottom of the conduction band is very much dominated by Ti 3*d* (Figure 5.4). The very strong Ti $2p_{3/2}$ and $2p_{1/2}$ core X-ray absorption features labeled C and G (in Figure 5.3) most

likely represent transitions to the unoccupied $3d_{5/2}$ and/or $3d_{3/2}$ states. Peaks D and H are expected to be the result of crystal field splitting, which is common in Ti^{4+} systems [16,18,19].

From the S 2*p* core level XAS spectra, in Figure 5.3c, we find that some features correspond to conduction band states which are aligned with Ti features, in either Figure 5.3a or 5.3b, indicative of unoccupied Ti states. This correlation, of S and Ti XAS features, indicates strong S to Ti 3*d* hybridization within the unoccupied density of states near the Fermi level. The alignment of the Ti 3*d* and S 3*p* orbitals approximately from 1 eV to 2.5 eV above the conduction band minimum has been predicted by theory [20-22], and this is indicated in the calculated band structure and partial density of states for TiS_3, shown in Figure 5.4. Furthermore, *p*-*d* hybridization has been observed for other transition-metal sulfides [23-24]. Thus, the S core edge XAS spectra is likely composed of features resulting from both S 2*p* → unoccupied S 4*s* - Ti 3*d* and S 2*p* → unoccupied S 3*p* - Ti 3*d* hybridized bands, although theory indicates the sulfur s weight to the unoccupied band structure just above the Fermi level is weak (Figure 5.4). Optically forbidden transitions, such *p* to *p* transitions, are allowed if there is hybridization [25].

The calculated TiS_3 band structure (Figure 5.4) shows a clear splitting between two sets of unoccupied bands: *lower* Ti-*d* and S-*p* hybrid bands and *upper* S-*s* and S-*p* hybrid bands. The bottom of the conduction band is mostly dominated by Ti-*d* bands, as has been noted above. S-*p* bands start contributing unoccupied density of states about 1 eV above the conduction band minimum and spans the rest of the lower part of the conduction band window. The *upper* part of the conduction band contains very narrow S-*p* band and delocalized hybrid S-*s* and S-*p* bands. The valance band on the other hand is much wider and dominated mostly by S-*p* and Ti-*d* orbitals.

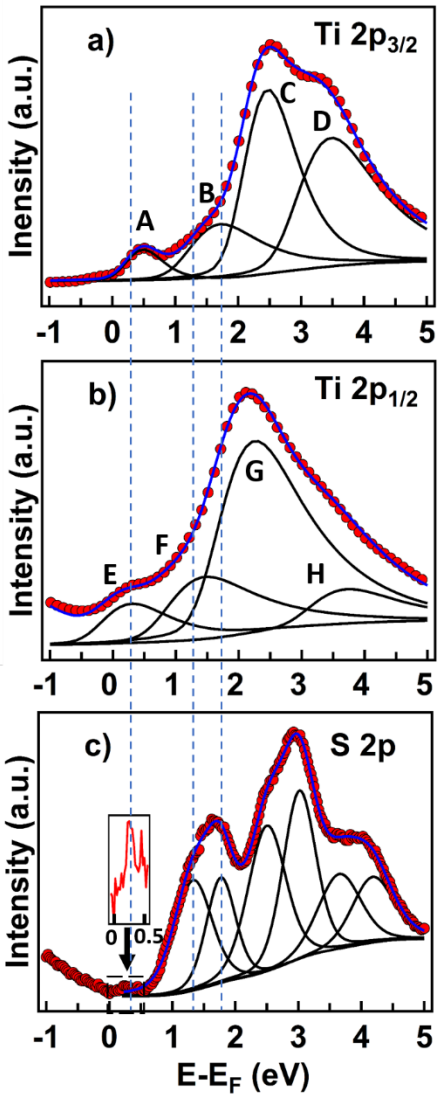

Figure 5.3 *The X-ray absorption edges for the a) Ti $2p_{3/2}$, b) Ti $2p_{1/2}$, and c) S 2p excitations in TiS_3. The inset in c) shows a minor feature located near the Fermi level. The placement of the Fermi level in c) is valid only for the first occurrence of each conduction band state indicated by the dotted lines. The red circles show experimental data, and the blue and black lines are the results of profile fitting. Data taken by Hemian Yi. Figure submitted for publication in S.J. Gilbert, H. Yi, A. Lipatov, A.J. Yost, T. Komesu, A. Sinitskii, J. Avila, M.C. Asensio, and P.A. Dowben, "Strong Metal-Sulfur Hybridization in the Conduction Band of the Quasi-One-Dimensional Transition Metal Trichalcogenides: TiS_3 and ZrS_3," Submitted to J. Phys. Chem. C*

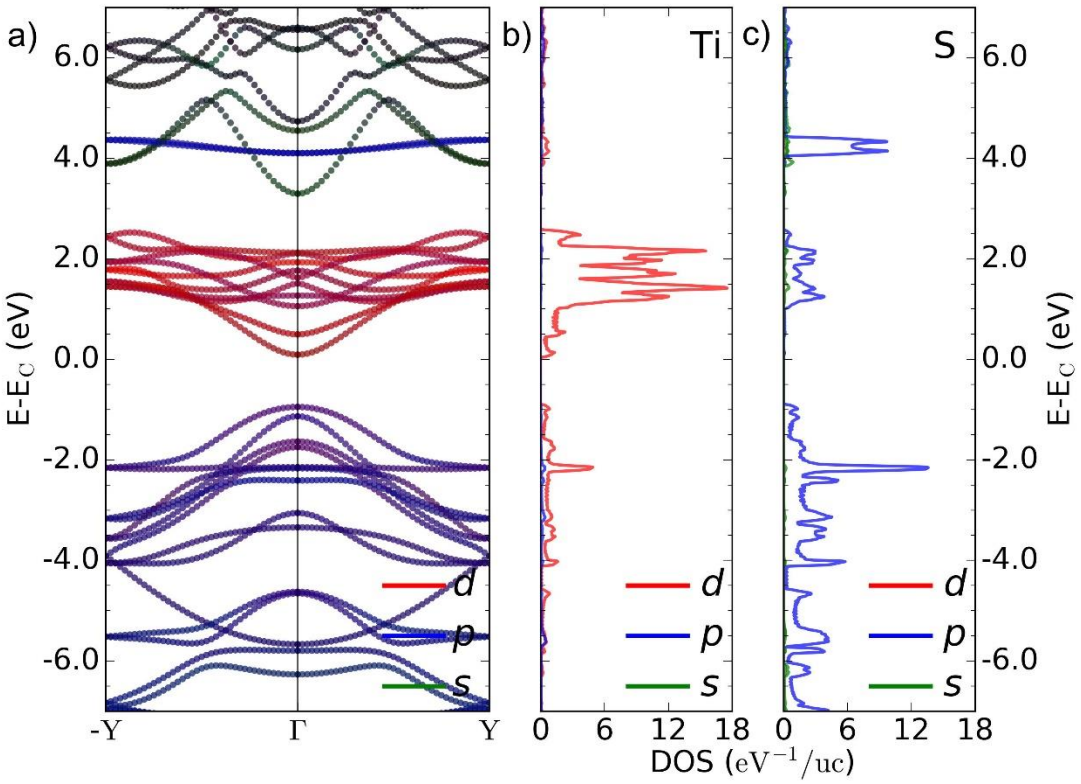

Figure 5.4 *The electronic structure of TiS_3 bulk (a). The band structure indicates the hybridization between Ti-d (red) and S-p (blue) orbitals in the valence and conduction bands. The bottom of conduction band has mostly Ti-d character. S-p bands start to contribute significantly ~ 1.0 eV above the conduction band minimum. The top of valence band has almost equal contribution from Ti-d and S-p bands. The adjoining orbital resolved partial density of states corresponding to Ti (b) and S (c) show the s orbital contribution is very small around the conduction and valence band edges. Calculations were done by Tula Paudel. Figure submitted for publication in S.J. Gilbert, H. Yi, A. Lipatov, A.J. Yost, T. Komesu, A. Sinitskii, J. Avila, M.C. Asensio, and P.A. Dowben, "Strong Metal-Sulfur Hybridization in the Conduction Band of the Quasi-One-Dimensional Transition Metal Trichalcogenides: TiS_3 and ZrS_3," Submitted to J. Phys. Chem. C*

5.4 The Conduction Band of ZrS_3

The XAS spectra taken at the Zr $3p_{3/2}$ and $3p_{1/2}$ core level edges, for ZrS_3, are presented in Figures 5.5a and 5.5b respectively. Both the Zr $3p_{3/2}$ and $3p_{1/2}$ edges are dominated by a single broad feature which was fit using 3 peaks located at 0.6, 1.9, and 3.2 eV above the Fermi level for the $3p_{3/2}$ edge and at 0.3, 1.3, and 2.7 eV for the $3p_{1/2}$. As with the Ti core level XAS features for TiS_3, the Zr transitions evident in Figures 5.5a and 5.5b are expected to be dominated by $p \rightarrow d$ transitions as indicated in the calculated partial density of states for the conduction band region of ZrS_3, as seen in Figure 5.6.

The XAS spectra taken at the S 2*p* core level edge, for ZrS_3, is shown in Figure 5.5c. Similar to the S 2*p* edge in TiS_3, the S 2*p* edge in ZrS_3 shows unoccupied S weighted states at roughly 0.3, 1.0, and 1.8 eV above the Fermi level. However, unlike in TiS_3, the transition to the state 0.3 eV above the Fermi level is significant. Because of this, the profile fitting requires three triplets rather than two. The three triplets are separated by 1.1-1.2 eV which is consistent with the separation between the core level states observed by XPS in Figure 5.2b. An additional tenth peak was required to fit a small shoulder feature at 4.8 eV.

The calculated ZrS_3 band structure (Figure 5.6) shows a single wide conduction band with the band width of the lower part of the conduction band now ~4 to 5 eV. The conduction band is dominated by Zr-*d* orbitals, even though S-*s* and S-*p* contribute. The S-*s* and S-*p* orbitals start contributing immediately above the conduction band minimum, more significantly by the latter. The valence band on the other hand is dominated by the S-*p* orbital, even though Zr-*d* orbitals make significant contributions to the valence band as well.

As with TiS_3, the three S weighted conduction band states of ZrS_3 appear hybridized with the transition-metal orbitals based on their energy alignment indicating either S 2*p* → S 4*s* - Zr 4*d* or S 2*p* → S 3*p* - Zr 4*d* transitions. The S 2*p* XAS transition to the unoccupied state near the Fermi

level has a more significant intensity for ZrS_3 (Figure 5.5c) than for TiS_3 (Figure 5.3c) where this transition to a similar unoccupied state near the Fermi level is barely evident. This indicates that the conduction band minimum in ZrS_3 contains more sulfur weight than is the case for TiS_3. This is consistent with our theoretical expectations (Figures 5.4 and 5.6), as just noted.

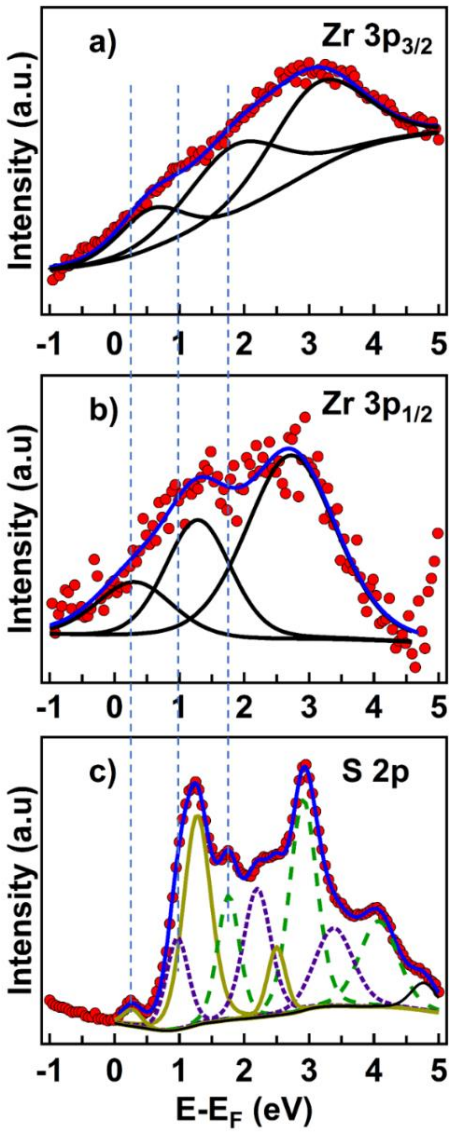

Figure 5.5 *The X-ray absorption edges for the a) Zr $3p_{3/2}$, b) Zr $3p_{1/2}$, and c) S 2p core excitations in ZrS_3. The placement of the Fermi level in c) is valid only for the first occurrence of each conduction band state indicated by the dotted lines. Green, purple and gold lines indicate excitations to the same conduction band state from the three distinct core level states. Data taken by Hemian Yi. Figure submitted for publication in S.J. Gilbert, H. Yi, A. Lipatov, A.J. Yost, T. Komesu, A. Sinitskii, J. Avila, M.C. Asensio, and P.A. Dowben, "Strong Metal-Sulfur Hybridization in the Conduction Band of the Quasi-One-Dimensional Transition Metal Trichalcogenides: TiS_3 and ZrS_3," Submitted to J. Phys. Chem. C*

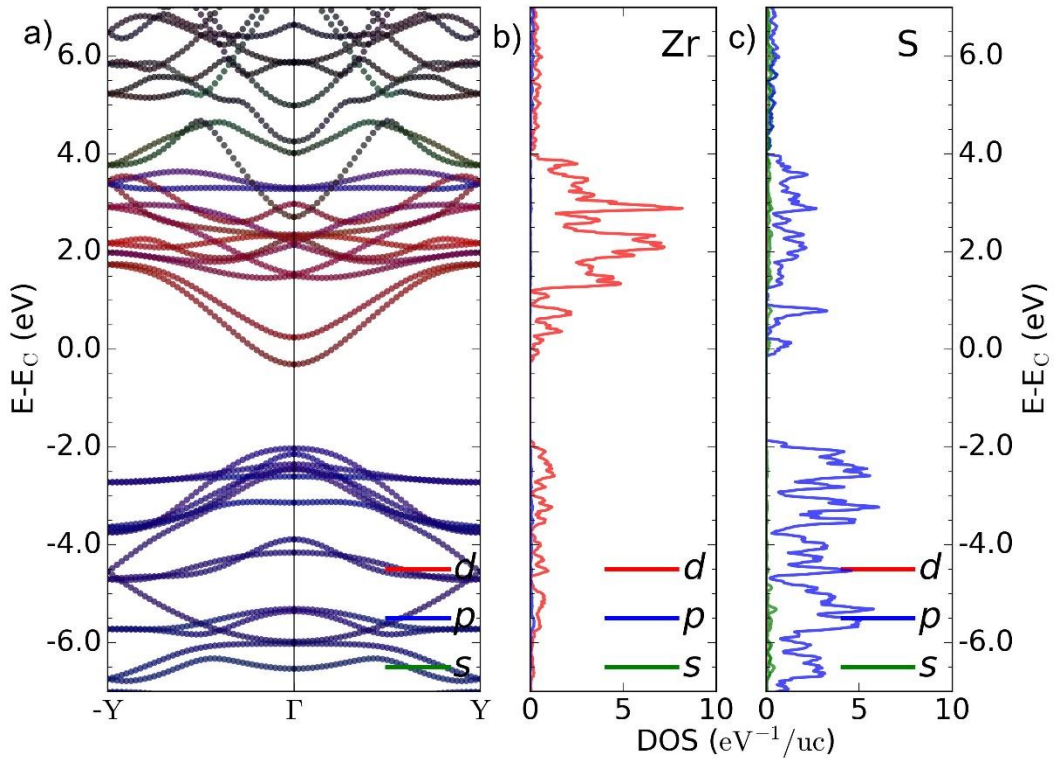

Figure 5.6 *The electronic structure of ZrS_3 bulk (a). The band structure illustrates the hybridization between Zr-d (red) and S-p (blue) orbitals in valence and conduction band. The bottom of conduction band has mostly Zr-d, however S-p and S-s orbitals start to contribute immediately above conduction band minimum. The top of valence band has almost equal contribution form Zr-d and S-p bands. Adjoining orbital resolved partial density of states corresponding to Zr (b) and S (c) show s and p orbital contribution to the conduction band edge is non-negligible. Calculations were done by Tula Paudel. Figure submitted for publication in S.J. Gilbert, H. Yi, A. Lipatov, A.J. Yost, T. Komesu, A. Sinitskii, J. Avila, M.C. Asensio, and P.A. Dowben, "Strong Metal-Sulfur Hybridization in the Conduction Band of the Quasi-One-Dimensional Transition Metal Trichalcogenides: TiS_3 and ZrS_3," Submitted to J. Phys. Chem. C*

5.5 Summary

As expected, the unoccupied states in the vicinity of the Fermi level of the conduction bands of TiS_3 and ZrS_3 are qualitatively similar. This was shown using X-ray absorption spectroscopy taken at the 2*p* core level edges of Ti and S, for TiS_3, and at the core level 2*p* edges of S and 3*p* edges of Zr, for ZrS_3. For both TiS_3 and ZrS_3, the unoccupied states of the conduction band within 2 eV of the Fermi level, appear dominated by either S s to Ti/Zr *d* or S *p* to Ti/Zr *d* hybridized orbitals. This sulfur to metal hybridization is expected to result in a partially delocalized electronic distribution between the Ti and S atoms within the same 1D chains, consistent with previous predictions [22]. The S atoms in both TiS_3 and ZrS_3 contribute appreciably to the electronic configuration between 1-2 eV above the Fermi level, but within 1 eV of the Fermi level the S contributions to the conduction band are very weak for TiS_3, and stronger for ZrS_3.

References

[1] J. A. McLeod, A. Buling, E. Z. Zurmaev, P. V. Sushko, M. Neumann, L. D. Finkelstein, S-W Kim, H. Hosono, and A. Moewes, *Phys. Rev. B.* **85**, 045204 (2012).

[2] S. J. Gilbert, A. Lipatov, A. J. Yost, M. J. Loes, A. Sinitskii, and P. A. Dowben, *Appl. Phys. Lett.* **114**, 101604 (2019).

[3] H. Yi, T. Komesu, S. Gilbert, G. Hao, A. J. Yost, A. Lipatov, A. Sinitskii, J. Avila, C. Chen, M. C. Asensio, and P. A. Dowben, *Appl. Phys. Lett.* **112**, 052102 (2018).

[4] M. E. Fleet, S. L. Harmer, X. Liu, and H. W. Nesbitt, *Surf. Sci.* **584**, 133 (2005).

[5] A. S. Shkvarin, Y. M. Yarmoshenko, M. V. Yablonskikh, A. I. Merentsov, and A. N. Titov, *J. Struct. Chem.* **55**, 1039 (2014).

[6] K. Endo, H. Ihara, K. Watanabe, and S-I Gonda, *J. Solid State Chem.* **44**, 268 (1982).

[7] F. Jellinek, R. A. Pollak, and M. W. Shafer, *Mater. Res. Bull.* **9**, 845 (1974).

[8] S. Artemkina, A. Poltarak, P. Poltarak, I. Asanov, and V. Fedorov, *Advances in Science, Technology and Engineering Systems Journal* **4**, 165 (2019).

[9] E. Flores, J. R. Ares, I. J. Ferrer, and C. Sánchez, *Phys. Status Solidi - Rapid Res. Lett.* **10**, 802 (2016).

[10] J. O. Island, M. Barawi, R. Biele, A. Almazán, J. M. Clamagirand, J. R. Ares, C. Sánchez, H. S. J. Van Der Zant, J. V. Álvarez, R. D'Agosta, I. J. Ferrer, and A. Castellanos-Gomez, *Adv. Mater.* **27**, 2595 (2015).

[11] A. Lipatov, P. M. Wilson, M. Shekhirev, J. D. Teeter, R. Netusil, and A. Sinitskii, *Nanoscale* **7**, 12291 (2015).

[12] A. J. Molina-Mendoza, J. O. Island, W. S. Paz, J. M. Clamagirand, J. R. Ares, E. Flores, F. Leardini, C. Sánchez, N. Agraït, G. Rubio-Bollinger, H. S. J. van der Zant, I. J. Ferrer, J. J. Palacios, and G. Castellanos-Gomez, *Adv. Funct. Mater.* **27**, 1605647 (2017).

[13] M. Randle, A. Lipatov, A. Kumar, C-P Kwan, J. Nathawat, B. Barut, S. Yin, K. He, N. Arabchigavkani, R. Dixit, T. Komesu, J. Avila, M. C. Asensio, P. A. Dowben, A. Sinitskii, U. Singisetti, and J. P. Bird, *ACS Nano* **13,** 803 (2018).

[14] N. V. Morozova, I. V. Korobeinikov, K. V. Kurochka, A. N. Titov, and S. V. Ovsyannikov, *J. Phys. Chem. C* **122**, 14362 (2018).

[15] H. Yi, S. J. Gilbert, A. Lipatov, A. Sinitskii, J. Avila, J. Abourahma, T. Komesu, M. C. Asensio, and P. A. Dowben, *J. Phys. Condens. Matter* **32**, 29LT01 (2020).

[16] G. van der Laan, and I. W. Kirkman, *J. Phys. Condens. Matter* **4**, 4189 (1992).

[17] M. Abdulsalam, and D. P. Joubert, *Eur. Phys. J. B* **88**, 177 (2015).

[18] F. M. F. de Groot, J. C. Fuggle, B. T. Thole, and G. A. Sawatzky, *Phys. Rev. B* **41**, 928 (1990).

[19] F. M. F. de Groot, J. C. Fuggle, B. T. Thole, and G. A. Sawatzky, *Phys. Rev. B* **42**, 5459 (1990).

[20] J. Dai and X. C. Zeng, *Angew. Chem.-Int. Ed.* **54**, 7572 (2015).

[21] S. Liu, W. Xiao, M. Zhong, L. Pan, X. Wang, H-X Deng, J. Liu, J. Li, and Z. Wei, *Nanotechnology* **29**, 184002 (2018).

[22] K. Taniguchi, Y. Gu, Y. Katsua, Y. Takafumi, and H. Takagi, *Appl. Phys. Express* **9**, 011801 (2016).

[23] A. V. Soldatov, A. N. Kravtsova, M. E. Fleet, and S. L. Harmer, *J. Phys. Condens. Matter* **16**, 7545 (2004).

[24] J. A. Tossell, *J. Chem. Phys.* **66**, 5712 (1977).

[25] Y. Sakisaka, T. N. Rhodin, and P. A. Dowben, *Solid State Comm.* **49**, 563 (1984).

6. Metal Contacts

As discussed in the introduction, metal contacts can have a profound impact on device performance, and, Schottky barrier formation due to incompatible contacts was one possible explanation for the discrepancy between the theoretical (~10,000 $cm^2\ V^{-1}\ s^{-1}$) [1] and experimentally measured (>100 $cm^2\ V^{-1}\ s^{-1}$) [2-6] electron mobilities. The convention for high work function metals, such as Au (5.1 eV [7] to 5.4 eV [8]) and Pt (5.5 eV [7,9,10] to 5.93 eV [11]), is that such metal contacts form Schottky barriers on n-type semiconductors [12], such as TiS_3 [13]. The Schottky barrier formation occurs as the result of upward band bending at the metal-semiconductor interface, and will be reflected in X-ray photoemission spectroscopy as a shift in the semiconductor's core level features toward lower binding energies [12,14].

6.1 A Search for Band Bending in TiS_3 with Au and Pt Adlayers

The X-ray photoemission spectra for the core level S 2p and Ti 2p photoelectron features with increasing Au and Pt coverage are shown in Figure 6.1. The Ti $2p_{3/2}$ and $2p_{1/2}$ core level features were fit with a single peak using a standard Voigt distribution function with a 70% Gaussian to 30% Lorentzian weighting; however, the S 2p core level spectra required multiple peaks, for any fitting, due to the distinct S environments in TiS_3. The two S environments (labeled S_2^{2-} and S^{2-}) are illustrated in Figure 6.2(a). Each S ion contributes two photoelectron core level features ($2p_{3/2}$ and $2p_{1/2}$) which are separated by 1.2 eV. Thus, the total spectrum contains 4 peaks as seen in Figure 6.2(b). However, the overlap of the S_2^{2-} $2p_{3/2}$ and S^{2-} $2p_{1/2}$ peaks causes the appearance of a triplet-like feature, with peak positions roughly at 161.1 eV, 162.3 eV, and 163.5 eV [13,15,16].

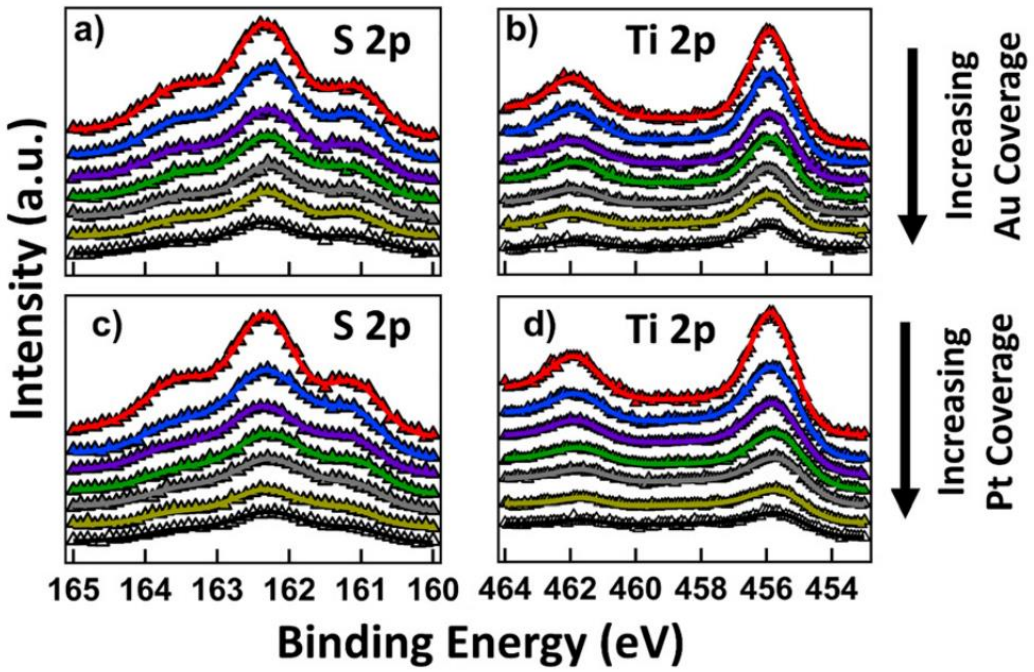

Figure 6.1 *The X-ray photoemission spectra of the S 2p and Ti 2p core level features in TiS_3, with increasing Au (a) and (b) or Pt (c) and (d) coverage. The triangles represent experimental data and solid lines are the result of profile fitting. Figure published in S.J. Gilbert, A. Lipatov, A.J. Yost, M.J. Loes, A. Sinitskii, and P.A. Dowben, Appl. Phys. Lett.* ***114****, 101604 (2019).*

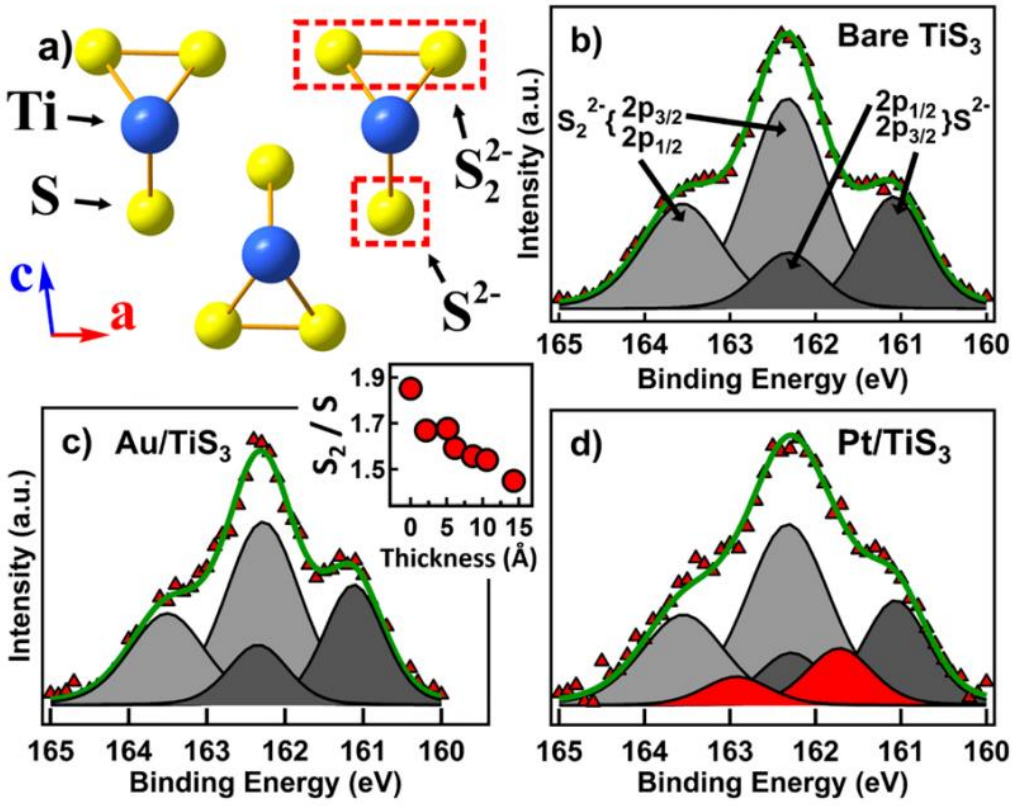

Figure 6.2 *(a) The atomic structure of TiS_3 highlighting different sulfur environments. (b) The individual S_2^{2-} (light gray) and S^{2-} (dark gray) peaks used to fit the S 2p XPS spectra for clean TiS_3. (c) The XPS fitting for TiS_3 with a 14 Å adlayer of Au. The inset shows the change in the S_2^{2-}/S^{2-} intensity ratio as a function of Au adlayer thickness. (d) The XPS fitting for TiS_3 with a 17 Å adlayer of Pt. Red peaks correspond to a Pt-S2-Ti environment at the interface. Figure published in S.J. Gilbert, A. Lipatov, A.J. Yost, M.J. Loes, A. Sinitskii, and P.A. Dowben, Appl. Phys. Lett.* ***114****, 101604 (2019).*

Figure 6.3 shows the measured Ti 2p and S 2p binding energies as the metal overlayer thickness is increased. In the case of Au on TiS_3, there is no observed binding energy shift for either the S 2p or Ti 2p photoelectron core level features. For Pt adlayers on TiS_3, the Ti 2p binding energies are reduced by ~0.25 eV, but the S 2p binding energies remain unchanged, with increasing Pt coverage. The near constant S 2p core level binding energies, evident in XPS, indicate that the shift to lower binding energies for the Ti 2p core level features, with increasing Pt coverage on TiS_3, is not related to the formation of a Schottky barrier, as will be discussed below. In fact, neither the Au/TiS_3 nor Pt/TiS_3 XPS data are consistent with the formation of a Schottky barrier.

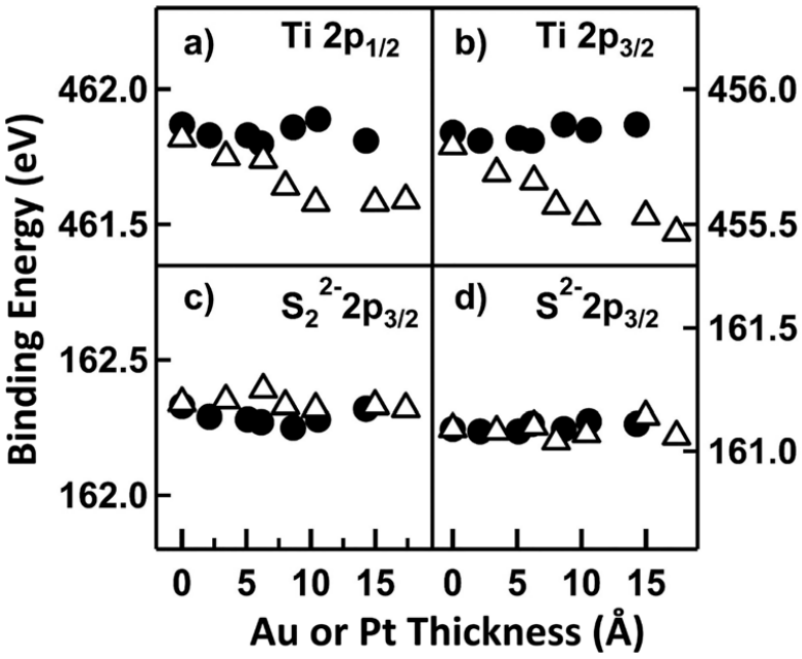

Figure 6.3 *The change in the Ti 2p and S 2p core level binding energies, as measured in XPS, for TiS_3 with increasing Au (black circles) or Pt (white triangles) coverage. Figure published in S.J. Gilbert, A. Lipatov, A.J. Yost, M.J. Loes, A. Sinitskii, and P.A. Dowben, Appl. Phys. Lett.* ***114****, 101604 (2019).*

6.2 Metal to Sulfur Bonding

The unexpected absence of a Schottky barrier can be explained through close examination of the S 2p photoelectron core level features. The topmost sulfur curves, red lines, in Figures 6.1(a) and 6.1(c), correspond to clean TiS_3 and were fit using the same parameters as our previous work using high resolution synchrotron measurements [13], as shown in Figure 6.2(b). For pure TiS_3, the ratio of the two types of sulfur species, S_2^{2-}:S^{2-}, is 2:1. As the metal coverage increases, the S_2^{2-}:S^{2-} ratio is expected to increase because the termination layer is composed of S_2^{2-} ions, and photoemission is surface sensitive. However, as the Au thickness increases, the S_2^{2-}:S^{2-} ratio decreases as seen in the inset of Figure 6.2(c). This indicates some form of Au-S interaction with the surface S_2^{2-} ions which reduces the S_2^{2-} XPS signal intensity. This interaction does not appear to be the formation of traditional bonds because there are no additional peaks in the S 2p fitting [Figure 6.2(c)] and the Ti 2p core level features appear unaffected by the Au-S interaction [Figures 6.3(a) and 6.3(b)]. On the other hand, the Pt/TiS_3 system shows indications of appreciable bonding at the metal-semiconductor interface. As the Pt coverage increases, the relative S_2^{2-} intensity once again decreases, but the shoulder-like S 2p core level features are also smoothed appreciably [Figure 6.2(d)]. As a result, the S 2p XPS data, obtained with increasing Pt coverage on TiS_3, cannot be fit well using only two doublets. For a proper fit of the S 2p features in the Pt/TiS_3 system, a third doublet [red peaks in Figure 6.2(d)] was introduced with peak positions at 161.7 eV and 162.9 eV. These peak positions are very similar to the S 2p core level features in TiS_2 [13] and are likely the result of a complex Pt-S2-Ti bonding environment. This is further indicated by the shift to lower binding energy for the Ti 2p core level features [Figures 6.3(a) and 6.3(b)], which indicates that the presence of Pt at the interface changes the Ti bonding environment. For both Au and Pt contacts, the metal-S interactions can explain the lack of a Schottky barrier, indicating that in these cases the interface chemistry is a more significant factor than the metal's work function.

6.3 Contact Resistance

To support these claims, we fabricated and tested a four-terminal TiS_3 field-effect transistor with Au contacts, for which TiS_3 was mechanically exfoliated and transferred onto a p-type silicon substrate with a 300 nm surface layer of SiO_2. A few layer thick TiS_3 whisker, approximately 30 nm in height and 0.11 μm wide, was selected for device fabrication. An atomic force microscopy (AFM) image of this TiS_3 whisker is shown in the top left inset in Figure 6.4(a). Au contacts were fashioned through electron-beam lithography and electron-beam evaporation, so that Au was in direct contact with the TiS_3 nanowhisker. The TiS_3 FET was placed in a Lake Shore (model TTPX) cryogenic probe station with a base pressure of about $2x10^{-6}$ Torr. The electrical characteristics of the device were recorded at room temperature using an Agilent 4155C semiconductor parameter analyzer. The scanning electron microscopy (SEM) image in the bottom right inset of Figure 6.4(a) shows the device, with the source (S), the drain (D), as well as V_1 and V_2 voltage probes labelled. In the field-effect measurements, the p-doped Si substrate served as a bottom gate (G) electrode. The main panel of Figure 6.4(a) presents the results of four-terminal measurements at zero gate bias, showing drain-source current (I_{DS}) as a function of drain-source voltage (V_{DS}; red curve) and as a function of the voltage drop between the V_1 and V_2 electrodes (V_{12}; blue curve), which was measured while V_{DS} was applied. Both I-V curves are linear, indicating Ohmic behavior rather than the presence of a Schottky barrier. The results are similar to the I-V curves obtained for TiS_3 FETs with Ti/Au and Cr/Au contacts [2,3,17,18]. The channel resistance measured in the four-terminal configuration was found to be R_{ch} = 1835 kΩ. With a channel length of 6.9 μm and a channel width of 0.11 μm [see the insets in Figure 6.4(a)], the calculated sheet resistance is about 29 kΩ/□. The estimated contact resistance at zero gate bias calculated from four-terminal measurements was found to be about 1 Ω*cm. This contact resistance is an order of magnitude lower than a MoS2 FET with Au contacts [19], which is believed to form a contact tunnel barrier of 1.03 eV [20]. In Figure 6.4(b), we plot transfer curves of the central segment of the TiS_3 device [inset in Figure 6.4(a)], which was measured in a two-terminal configuration, when the current through the central

segment was measured while applying a potential difference directly between the V_1 and V_2 electrodes, and a four-terminal configuration, when the outer S and D electrodes were used to source current through the TiS_3 crystal, and the inner electrodes were used to measure the V_2-V_1 potential difference. The devices exhibited a hysteresis in the electronic transport, which is similar to those previously reported in the studies of TiS_3 FETs [2,18] as well as for devices based on various 2D materials, such as graphene [21,22] and MoS_2 [23], on oxide substrates. The hysteresis I-V curves in these devices are typically associated with the interfacial charge traps i.e., charge trapping. From the graphs in Figure 6.4(b), the maximum electron mobility (μ_e) was extracted and found to be 11 $cm^2\ V^{-1}\ s^{-1}$ and 12 $cm^2\ V^{-1}\ s^{-1}$ in the two- and four-terminal configurations, respectively. The difference in the electron mobility between different configurations is negligible indicating that the contact resistance present in the two-terminal configuration is not a significant factor in determining the electronic characteristics of the TiS_3 channel. Another TiS_3 device prepared simultaneously with the presented one, but in only the two-terminal configuration, showed an electron mobility of 27 $cm^2\ V^{-1}\ s^{-1}$, which is comparable to values obtained for devices with Cr/Au and Ti/Au contacts [2,3,5].

To estimate the charge carrier concentration (n), we used the following relationship, $\sigma = n\ e\ \mu_e$, where σ is the electrical conductivity and e is the electron charge. For the presented device, this relationship yielded n ranging from ~6 × to 8 × 10^{18} cm^{-3} for different gate voltages (V_G), which is in very good agreement with the previously reported estimate of the doping concentration of 7 × 10^{18} cm^3 obtained by analyzing the transfer characteristics of TiS_3 FETs using density functional perturbation theory (DFPT) [18]. The I_{DS}-V_{DS} curves remained linear as the V_G changed from -80 to 80 V, suggesting no appreciable effect of the gate voltage modulation and the associated variation of the carrier concentration on the contact resistance.

The fact that Ohmic contacts do not vastly improve the electron mobility indicates that the contact resistance is not always the dominant factor leading to a reduction in the measured electron mobility. Other factors such as the substrate choice, the electron-phonon coupling [18], etc., must

be explored in order to explain the discrepancy between the theoretical (~10,000 $cm^2 V^{-1} s^{-1}$) [1] and experimentally measured (>100 $cm^2 V^{-1} s^{-1}$) [2-6] electron mobility in TiS_3.

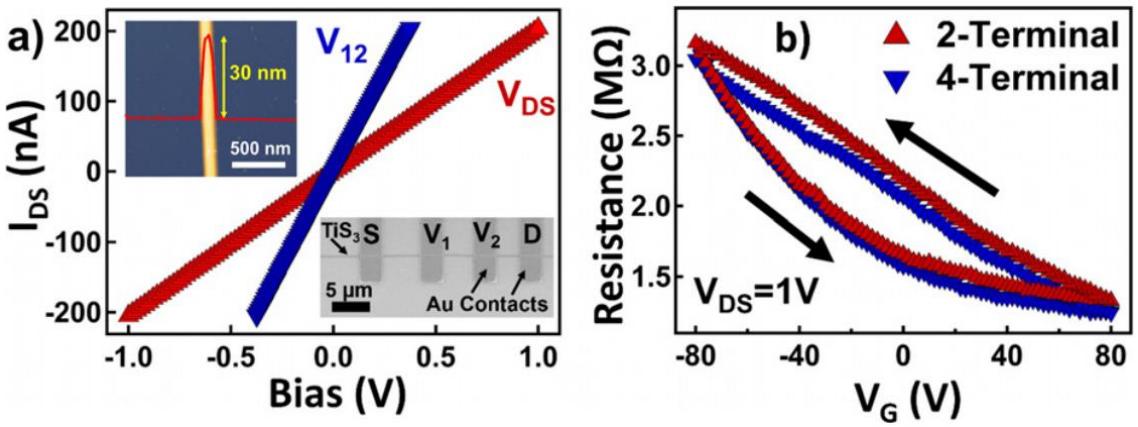

Figure 6.4 *(a) The I-V curves obtained from four-terminal measurements of a TiS_3 FET with Au electrodes at zero gate bias. The top left inset shows the AFM image of the TiS_3 whisker used for the device fabrication. The image is overlaid with an AFM height profile (red line) across the TiS_3 whisker showing its height to be about 30 nm. The bottom right inset shows the SEM image of the TiS_3 device. (b) The resistance as a function of gate voltage in both the 2-terminal (red) and 4-terminal (blue) configurations for the same TiS_3 device segment. AFM taken by Michael Loes. Device measurements taken by Alexey Lipatov. Figure published in S.J. Gilbert, A. Lipatov, A.J. Yost, M.J. Loes, A. Sinitskii, and P.A. Dowben, Appl. Phys. Lett.* ***114****, 101604 (2019).*

6.4 Summary

XPS provides clear indications that the contact metals Au and Pt experience strong interface interactions with sulfur in TiS_3(001). These strong interactions may be why Schottky barrier formation is suppressed for Au or Pt on TiS_3(001), in spite of the high work function of these metals. Additionally, device measurements show negligible contact resistance between Au and TiS_3. However, the electron mobility measured, using Au contacts, was not found to be significantly higher than what was measured in other TiS_3 devices, where Schottky barrier formation is present. A small contact resistance or Schottky barrier, on the order of a few meV, as reported for Cr/Au contacts on TiS_3 [18], cannot a priori be excluded on the basis of the measurements reported here, but any such Schottky barrier would have minimal effects on room temperature device performance.

References

[1] J. Dai and X. C. Zeng, *Angew. Chem., Int. Ed.* **54**, 7572 (2015).

[2] A. Lipatov, P. M. Wilson, M. Shekhirev, J. D. Teeter, R. Netusil, and A. Sinitskii, *Nanoscale* **7**, 12291 (2015).

[3] J. O. Island, M. Barawi, R. Biele, A. Almazan, J. M. Clamagirand, J. R. Ares, C. Sanchez, H. S. J. Van Der Zant, J. V. Alvarez, R. D'Agosta, I. J. Ferrer, and A. Castellanos-Gomez, *Adv. Mater.* **27**, 2595 (2015).

[4] A. J. Molina-Mendoza, J. O. Island, W. S. Paz, J. M. Clamagirand, J. R. Ares, E. Flores, F. Leardini, C. Sanchez, N. Agraıt, G. Rubio-Bollinger, H. S. J. van der Zant, I. J. Ferrer, J. J. Palacios, and A. Castellanos-Gomez, *Adv. Funct. Mater.* **27**, 1605647 (2017).

[5] J. O. Island, R. Biele, M. Barawi, J. M. Clamagirand, J. R. Ares, C. Sanchez, H. S. J. Van Der Zant, I. J. Ferrer, R. D'Agosta, and A. Castellanos-Gomez, *Sci. Rep.* **6**, 22214 (2016).

[6] E. Finkman and B. Fisher, *Solid State Commun.* **50**, 25 (1984).

[7] D. E. Eastman, *Phys. Rev. B* **2**, 1 (1970).

[8] H. C. Potter and J. M. Blakely, *J. Vac. Sci. Technol.* **12**, 635 (1975).

[9] D. M. Collins, J. B. Lee, and W. Spicer, *Surf. Sci.* **55**, 389 (1976).

[10] R. I. Mints, V. P. Melekhin, and M. B. Partenskii, *Sov. Phys. Solid State* **16**, 2330 (1975).

[11] P. E. C. Franken and V. Ponec, *Surf. Sci.* **53**, 341 (1975).

[12] Z. Zhang and J. T. Yates, *Chem. Rev.* **112**, 5520 (2012).

[13] H. Yi, T. Komesu, S. Gilbert, G. Hao, A. J. Yost, A. Lipatov, A. Sinitskii, J. Avila, C. Chen, M. C. Asensio, and P. A. Dowben, *Appl. Phys. Lett.* **112**, 052102 (2018).

[14] E. Echeverrıa, G. Peterson, B. Dong, S. Gilbert, A. Oyelade, M. Nastasi, J. A. Kelber, and P. A. Dowben, *Z. Fur Phys. Chem.* **232**, 893 (2018).

[15] M. E. Fleet, S. L. Harmer, X. Liu, and H. W. Nesbitt, *Surf. Sci.* **584**, 133 (2005).

[16] K. Endo, H. Ihara, K. Watanabe, and S.-I. Gonda, *J. Solid State Chem.* **44**, 268 (1982).

[17] J. O. Island, M. Buscema, M. Barawi, J. M. Clamagirand, J. R. Ares, C. Sanchez, I. J. Ferrer, G. A. Steele, H. S. J. van der Zant, and A. Castellanos-Gomez, *Adv. Opt. Mater.* **2**, 641 (2014).

[18] M. Randle, A. Lipatov, A. Kumar, C.-P. Kwan, J. Nathawat, B. Barut, S. Yin, K. He, N. Arabchigavkani, R. Dixit, T. Komesu, J. Avila, M. C. Asensio, P. A. Dowben, A. Sinitskii, U. Singisetti, and J. P. Bird, *ACS Nano* **13**, 803 (2019).

[19] S.-L. Li, K. Komatsu, S. Nakaharai, Y.-F. Lin, M. Yamamoto, X. Duan, and K. Tsukagoshi, *ACS Nano* **8**, 12836 (2014).

[20] I. Popov, G. Seifert, and D. Tomanek, *Phys. Rev. Lett.* **108**, 156802 (2012).

[21] H. Wang, Y. Wu, C. Cong, J. Shang, and T. Yu, *ACS Nano* **4**, 7221 (2010).

[22] A. Lipatov, A. Fursina, T. H. Vo, P. Sharma, A. Gruverman, and A. Sinitskii, *Adv. Electron. Mater.* **3**, 1700020 (2017).

[23] D. J. Late, B. Liu, H. S. S. R. Matte, V. P. Dravid, and C. N. R. Rao, *ACS Nano* **6**, 5635 (2012).

7. Applications in the Field of Spintronics

In addition to field-effect and phototransistor devices, the transition metal trichalcogenides are particularly appealing for the creation of spintronic devices which utilize the proximity effect [1], as mentioned in the introduction. Mean field theory [2-5] indicates that the induced polarization, due to the proximity effect, of the paramagnetic overlayer will decay away from the interface with the length scale of the paramagnetic correlation length, so a 2D channel will retain a higher polarization than a thicker semiconductor layer [6]. In this Chapter, one example of a device based on the proximity effect will be discussed along with measurements that highlight the potential for the transition metal trichalcogenides for use as the transistor channel in these devices.

7.1 Antiferromagnetic Spin-Orbit Read Logic

The concept for an antiferromagnetic spin-orbit read (AFSOR) logic device is illustrated in Figure 7.1. A 2D material with appreciable spin-orbit coupling is placed at the interface of an antiferromagnetic magnetoelectric with net boundary magnetization, such as Cr_2O_3, and the boundary magnetization will induce a spin-polarization in the 2D material [1]. Because of the spin-orbit coupling in the material, the spin-up and spin-down electrons will have a positive and negative k-vector, respectively, at the bottom of the conduction band. When the spin-up and spin-down bands are split due to the interface magnetization, the majority spin state will now have a net positive or negative k-vector resulting in a high resistance traveling toward the drain and a low resistance traveling toward the source, or visa versa [1]. The two resistance states can be switched by switching the magnetization of the underlying substrate as is illustrated in Figure 7.1c.

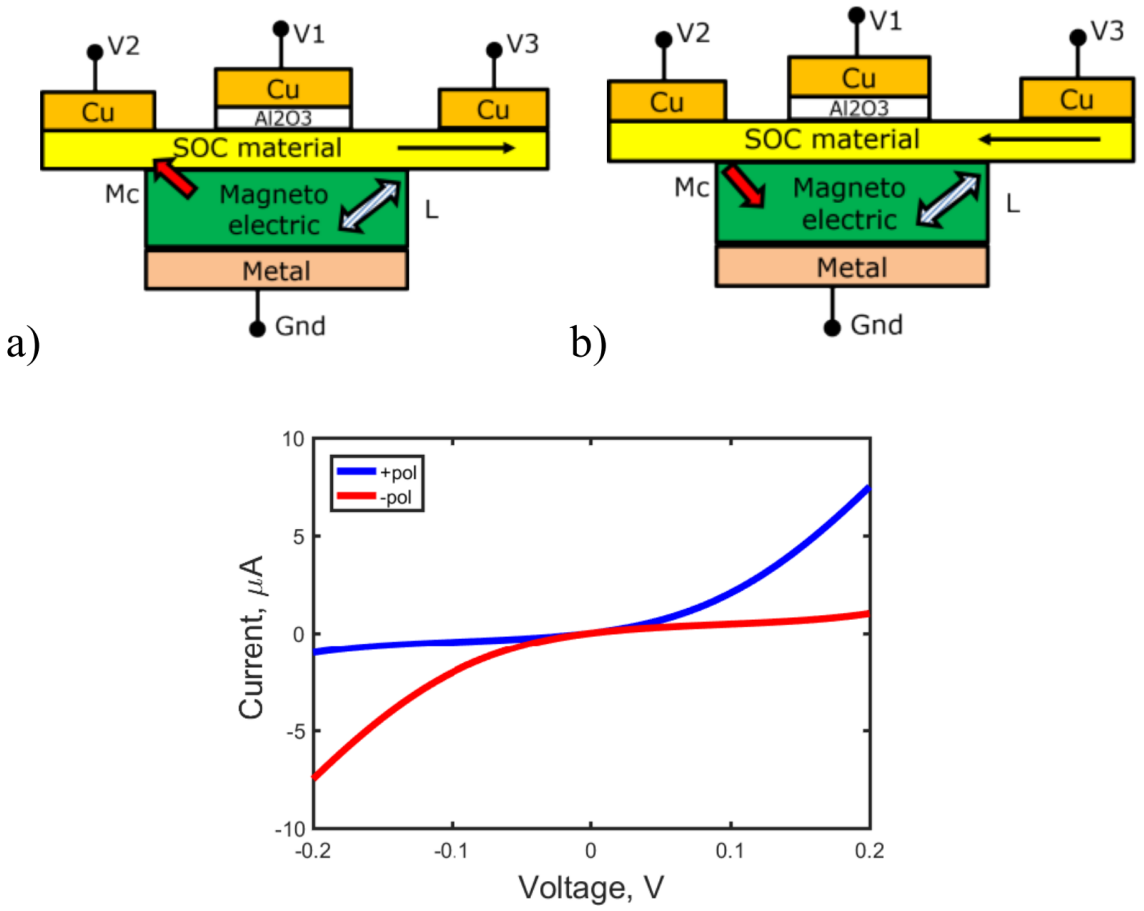

Figure 7.1 *Scheme of AFSOR logic. (a) State with positive V_1 applied and the surface or interface magnetization of the ME gate M_{surf} pointing up. (b) State with negative V_1 applied and surface magnetization M_{surf} pointing down. C) Source to drain current versus voltage V_1 in the AFSOR device with the SOC channel polarized in opposite directions (+ or −) by the ME gate. Figure adapted from [1] with permission from P. A. Dowben.*

7.2 Symmetry Protected Photocurrents

The X-ray diffraction (XRD) measurements on TiS_3, which were shown in Figure 2.1, indicate that TiS_3 nano-whiskers conform to a monoclinic structure, with space group: $P2_1/m$, and lattice constants of a = 4.9728(6) Å, b = 3.4055(4) Å, c = 8.8146(15) Å and a cant angle of β = 97.56(1)°. This data suggests that the bulk crystal is centrosymmetric, but the surface cannot possess inversion symmetry as $\beta \neq 90°$. The presence of broken symmetry at the surface such that the surface exhibits a non-centrosymmetric environment, as compared to the centrosymmetric bulk crystal, allows for the possibility of spin-orbit coupling of the surface weighted electronic structure. In a previous study [7], measurements of the valence band energy-momentum dispersion in TiS_3(001) along $\bar{\Gamma}$ to $\bar{Y}$ and along $\bar{\Gamma}$ to $\bar{B}$ indicate that although the crystal nominally exhibits $P2_1/m$ symmetry, the surface Brillioun zone lacks mirror plane inversion symmetry, in agreement with the hypothesis produced from single crystal XRD analysis. The absence of the inversion symmetry at the surface is indicated in the constant energy contour photoemission intensity plots [8] and in detailed analysis of the crystal structure (i.e. a non rectilinear cant angle) that suggests an absence of perfect mirror symmetry at the surface when travelling along the critical points. The lack of mirror plane inversion symmetry at the surface suggests, as noted above, that there should be some spin-orbit coupling in the valence band structure [9]. Based on these findings, TiS_3 may provide sufficient spin-orbit coupling to create AFSOR devices.

To examine the possibility of generating a symmetry protected current in a TiS_3 transistor channel, scanning photocurrent microscopy (SPCM) was performed using circularly polarized light. The SPCM images are shown in Figure 7.2. By utilizing circularly polarized light, the different spin states can be selectively excited [10-12], and if the spin states are split by spin orbit coupling, this should result in a photocurrent with a positive or negative k-vector as illustrated in Figure 7.3a. When right circularly polarized light was used, the photocurrent production was enhanced traveling toward the source and diminished traveling toward the drain (when compared

to the photocurrent using left circularly polarized light) as seen in Figure 7.3b. This is consistent with the expectations for a symmetry protected photocurrent and indicates even the low Z value transition metal trichalcogenides, such as TiS_3, may be suitable for AFSOR devices.

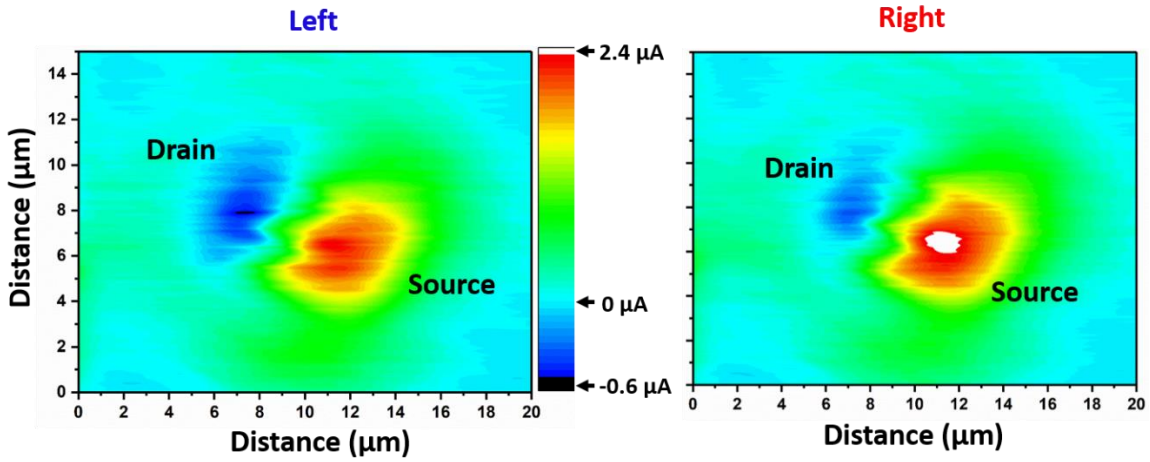

Figure 7.2 *Scanning photocurrent microscopy images of a TiS_3 phototransistor channel using circular left and circular right polarized light.*

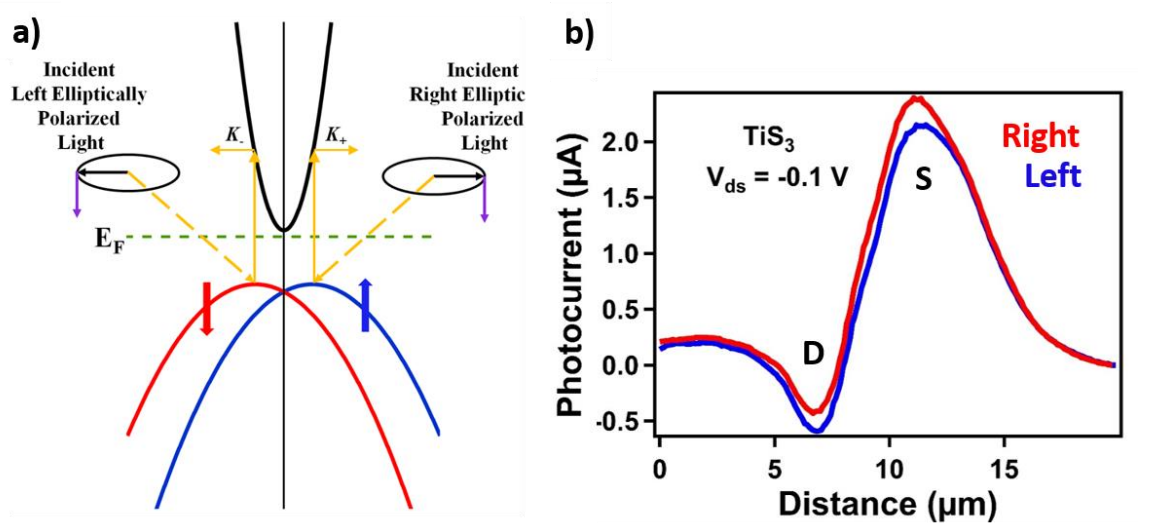

Figure 7.3 *a) An illustration of using circularly polarized light to excite specific spin states in a material with appreciable spin-orbit coupling. b) The photocurrent produced along a TiS_3 transistor channel using different light polarizations.*

7.3 Spin Polarization via the Proximity Effect

For use in and AFSOR device, the conduction band states must be spin polarized via the proximity effect, rather than through excitations with circularly polarized light. In order to, verify that this could be achieved using TiS_3, a TiS_3 crystal was exfoliated in ultra-high vacuum (UHV) and then transferred *in-situ* to a UHV cleaned Cr_2O_3 substrate which produces a pristine interface between the 2D material and the antiferromagnetic substrate. Photoemission electron microscopy (PEEM) coupled with X-ray magnetic circular dichroism (XMCD) was then performed at the Ti 2p edge to measure any spin-polarization in the conduction band of TiS_3 (Figure 7.4). As can be seen in Figure 7.4b, the intensity is significantly altered when using circular left or circular right polarizations, even at room temperature, suggesting that the conduction band states in TiS_3 may be spin polarized via the proximity effect even at room temperature.

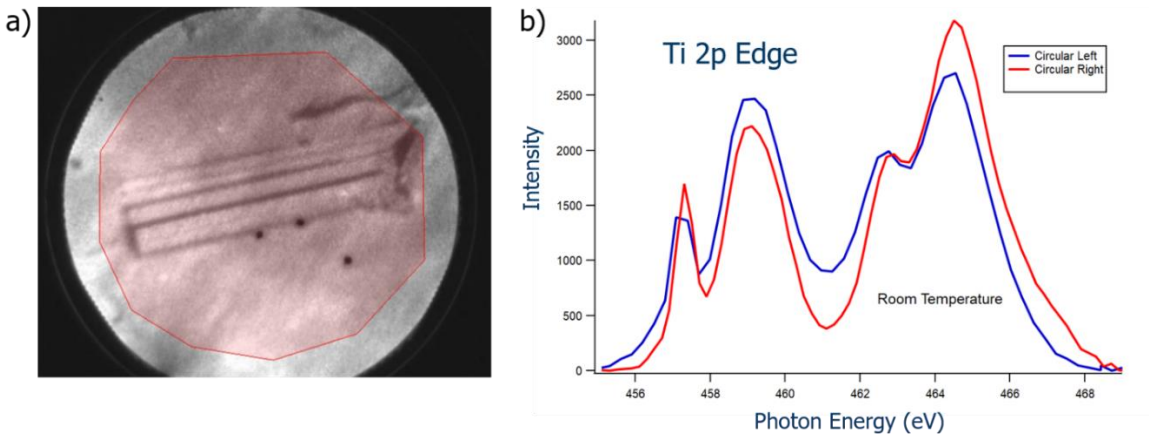

Figure 7.4 *a) A PEEM image of a TiS_3 ribbon on a Cr_2O_3 substrate. b) The XMCD signal taken in the red area of a). The data shown here was taken by Jian Wang.*

7.4 Summary

The transition metal trichalcogenides are promising candidates for spintronic devices utilizing the proximity effect. These measurements show that TiS_3 with a relatively low Z value is still capable of providing the spin-orbit coupling splitting necessary to create symmetry protected photocurrents which could be used in AFSOR devices even at room temperature. TMTs with larger Z values, such as $ZrSe_3$ and HfS_3, will likely provide larger spin-orbit coupling splitting which could maximized the on off ratios in these spintronic devices.

References

[1] P. A. Dowben, C. Binek, K. Zhang, L. Wang, W-N Mei, J. P. Bird, U. Singisetti, X. Hong, K. L. Wang, and D. Nikonov, *IEEE J. Explor. Solid State Comput. Dev. Circ*. **4**, 1 (2018).

[2] P. A. Dowben, D. Lagraffe, D. Li, A. Miller, L. Zhang, L. Dottl, and M. Onellion, *Phys. Rev. B* **43**, 3171 (1991).

[3] J. Mathon, *J. Phys.: F: Met. Phys.* **16**, L217 (1986).

[4] F. Fishman, F. Schwabl, and D. Schwenk, *Phys. Lett. A* **121**, 192 (1987).

[5] D. Schwenk, F. Fishman, and F. Schwabl *Phys. Rev. B* **38**, 11618 (1988).

[6] S. J. Gilbert and P. A. Dowben, *J. Phys. D: Appl. Phys*. **53**, 343001 (2020).

[7] H. Yi, T. Komesu, S. Gilbert, G. Hao, A. J. Yost, A. Lipatov, A. Sinitskii, J. Avila, C. Chen, M. C. Asensio, P. A. Dowben, *Appl. Phys. Lett.* **2018**, *112*, 052102.

[8] S. Furuseth, L. Brattås, A. Kjekshus, *Acta Chem. Scand. A* **1975**, *29*, 623.

[9] E. Rashba, *Sov. Phys.-Solid State* **1960**, *2*, 1109.

[10] N. Wu, X. He, A. L. Wysocki, U. Lanke, T. Komesu, K. D. Belashchenko, C. Binek, and P. A. Dowben *Phys. Rev. Lett.* **106**, 087202 (2011).

[11] S. Cao, M. Street, J. Wang, J. Wang, X. Zhang, C. Binek, and P. A. Dowben *J. Phys. Condens. Matter* **29**, 10LT01 (2017)

[12] C. T. Chen, Y. U. Idzerda, H. J. Lin, N. V. Smith, G. Meigs, E. Chaban, G. H. Ho, E. Pellegrin, and F. Sette *Phys. Rev. Lett.* **75**, 152 (1995).

8. Conclusions and Future Studies

The transition metal trichalcogenides have been studied here for their potential in the fields of nanoelectronics, optoelectronics, and spintronics. The quasi-1D structure exhibited by the TMTs results in superior edge termination as well as a preferred charge transport direction which enables the scaling of electronic devices to widths below 10 nm without the devastating edge scattering effects seen in other 2D materials. Furthermore, the 1D structure also produces a remarkable light polarization sensitivity in these materials when used as phototransistors enabling the production of polarization sensitive photodetectors for visible and near infrared wavelengths. The TMTs have many promising attributes for electronic devices including Ohmic contacts with Au and Pt and sufficient spin-orbit coupling to produce symmetry protected currents; however, the electron mobilities remain low, and the strong metal-sulfur hybridization my result in unanticipated challenges when doping these materials.

The devices studied here were fabricated by mechanically exfoliating TiS_3 and ZrS_3 whiskers onto SiO_2 substrates. However, for any commercial applications, large scale monolayer or few-layer growth will need to be achieved in a controlled manner. Future work might well be profitable if directed towards realizing monolayer coverage on SiO_2 as well as on magnetic insulators such as EuO, EuS, yttrium iron garnet and Cr_2O_3 which could be used to create spintronic devices. Additionally, while the studies here indicate a spin-polarization via the proximity effect for TiS_3 on Cr_2O_3 a working device in which the transistor channel is spin-polarized through interactions with a magnetoelectric antiferromagnet has not yet been achieved. Furthermore, studies on the higher Z value transition metal trichalcogenides which should maximize the spin-orbit coupling splitting, such as $ZrSe_3$ HfS_3, are lacking and should be the focus of future research.

While we have found that Au and Pt produce Ohmic contacts on TiS_3, the contacts issues cannot explain the electron mobilities which remain two orders of magnitude below the theoretical predictions. It is likely that this discrepancy is caused by phonon scattering which was not account

for in the theory [1]. Overlayers of Al_2O_3 have been found to increase the electron mobility [2] likely due to the suppression of phonon modes. Reducing the sample dimensions as well as investigating other overlayer materials may further suppress the phonon modes and increase the electron mobility. Such advances would not only be beneficial for the transistor devices discussed here, but also for potential thermoelectric devices using the transition metal trichalcogenides. It has been predicted that TMTs such as TiS_3, ZrS_3, and $ZrSe_3$ monolayers could be promising thermoelectric candidates [3-5]; however, experiments have found their performance lacking, largely due to their high resistivity [6]. Since reducing both the thermal conductivity and electrical resistivity is desirable for thermoelectric applications, investigating methods to suppress the phonon modes while also increasing the electron mobility would be valuable for thermoelectric devices in addition to the devices discussed here.

References

[1] M. Randle, A. Lipatov, A. Kumar, C-P Kwan, J. Nathawat, B. Barut, S. Yin, K. He, N. Arabchigavkani, R. Dixit, T. Komesu, J. Avila, M. C. Asensio, P. A. Dowben, A. Sinitskii, U. Singisetti, and J. P. Bird, *ACS Nano* **13,** 803 (2018).

[2] A. Lipatov, P. M. Wilson, M. Shekhirev, J. D. Teeter, R. Netusil, and A. Sinitskii, *Nanoscale* **7**, 12291 (2015).

[3] J. Zhang, X. Liu, Y. Wen, L. Shi, R. Chen, H. Liu, and B. Shan, *ACS Appl. Mater. Interfaces* **9**, 2509 (2017).

[4] Z. Zhou, H. Liu, D. Fan, G. Gao, and C. Sheng, *ACS Appl. Mater. Interfaces* **10**, 37031 (2018).

[5] C. Wang, C. Zheng, and G. Gao, *J. Phys. Chem. C* **124**, 6536 (2020).

[6] E. Guilmeau, D. Berthebaud, P. R. N. Misse, S. Hebert, O. I. Lebedev, D. Chateigner, C. Martin, and A. Maiganan, *Chem. Mater.* **26**, 5585 (2014).